The old, unique C1 chondrite Flensburg – Insight into the first processes of aqueous alteration, brecciation, and the diversity of water-bearing parent bodies and lithologies

Electronic Annex - Supplemental Materials

More details on the fall observations, recovery and further search

After the fireball observation (Fig. S1) the Maritime Rescue Coordination Centre Bremen of the German Maritime Search and Rescue Service (DGzRS) received several reports from ships in the North Sea and initially considered the bolide to be an emergency signal between the East Frisian Islands of Langeoog und Spiekeroog. They sent two inshore lifeboats into the area.

One day after the fireball event at around 11 am local time (CEST), Mr. Due-Hansen found the peculiar stone on top of the grass and he instantly remembered the news about the meteor over the North Sea the day before. He considered it to be unusual for a stone, to lie on top of the lawn and, therefore, suspected it had fallen from the sky. At the weekend he took the stone to his father in Denmark and showed it to some friends as well. Accordingly, the meteorite was touched by several people. The finder declared that he had used a strong magnet for testing the stone’s ferromagnetic reaction, which was positive. It should also be mentioned that between the time the fireball was observed and the discovery, several millimeters of rain as well as elevated relative humidity were reported in Flensburg.

After reporting the meteorite find to the International Meteor Organization (IMO) website, Mr. Due-Hansen sent four pictures of the stone to the American Meteor Society operations manager Mike Hankey. In order to consult local experts in Germany, Mr. Hankey contacted the Arbeitskreis Meteore (AKM) and got in touch with meteorite specialist Dieter Heinlein, coordinator of the German Fireball Network of the DLR (Deutsches Zentrum für Luft- und Raumfahrt) for a scientific examination of the stone.

Two AKM members Laura Kranich and Carsten Jonas, who are based in Kiel, visited Erik Due-Hansen and his wife on September 27. They precisely measured and documented the finding site (54°45.6873' N, 9°22.7353' E = 54.761455° N, 9.378922° E) and interviewed the couple concerning the circumstances of the discovery. Finally, the finder handed over the golf ball-sized rock to Laura and Carsten, who immediately sent the small meteorite by priority mail to Augsburg for a detailed inspection by Dieter Heinlein. The Flensburg meteorite is a complete individual weighing 24.5 grams and showing a very fresh black fusion crust with many contraction cracks. On a few patches, where the primary crust had been broken off, a thin layer of brownish (ochre-colored) secondary fusion crust is visible. A small physical scratch implies that the meteorite must have scraped a hard surface before it smoothly landed on the lawn of Mr. Due-Hansen's property.

On November 11 the 24.5 g Flensburg stone was delivered to the Institut für Planetologie in Münster for analysis and cutting into two major pieces of 17.03 g and 6.54 g.

Soon after the first meteorite find was confirmed and released, various searching activities in the Flensburg area were undertaken by AKM members and other parties, but, unfortunately, no further genuine meteorite piece was found. Several groups (Mike Hankey of the American Meteor Society, Laura Kranich and Carsten Jonas of AKM, as well as Jim Goodall from Michigan, USA) tried to calculate the bolide's luminous trajectory and the potential strewn field with different results.
This turned out to be a challenging problem, which only could be solved by sophisticated calibrations of some video records of the daylight fireball with night time images through Felix Bettonvil and Gerd Baumgarten. This fundamental spadework enabled Czech experts Jiří Borovička and Pavel Spurný, Ondřejov Observatory to determine the atmospheric path (Fig. S1) and the strewnfield of the multiple meteorite fall properly. Detailed results of these investigations will be published elsewhere in a separate paper.

Samples and Analytical procedures

Optical and electron microscopy

Several thin and thick sections of Flensburg (PL19171 (~71 mm^2), PL19172 (~132 mm^2) (PL19173 (~ 13 mm^2), PL19174 (~16 mm^2); Institut für Planetologie, Münster) were studied by optical and electron optical microscopy. A ZEISS polarizing microscope (Axiophot) was used for optical microscopy in transmitted and reflected light. To study the fine-grained textures and to identify the different mineral phases, a JEOL 6610-LV electron microscope (SEM) at the Interdisciplinary Center for Electron Microscopy and Microanalysis (ICEM) at the Westfälische Wilhelms-Universität Münster was used.

In an area of 15 mm², the size and abundance of relict chondrules have been measured 7 times by 4 different persons on a BSE map. The average sizes of relict chondrules range from ~126 (including all rounded objects as possible relict chondrules) to ~194 µm (only including the absolutely safe objects) with minimum and maximum sizes of ~25 µm and ~685 µm, respectively, in each run. On average, 134 relict chondrules have been measured with a size of 168 µm.

Chemical analyses using microprobe and SEM-EDS

Quantitative mineral and bulk analyses were obtained using a JEOL JXA 8530F electron microprobe (EPMA) at the Institut für Mineralogie in Münster, which was operated at 15 kV and a probe current of 15 nA. Natural and synthetic standards were used for wavelength dispersive spectrometry. Jadeite (Na), kyanite (Al), sanidine (K), chromium oxide (Cr), San Carlos olivine (Mg), hypersthene (Si), diopside (Ca), rhodonite (Mn), rutile (Ti), fayalite (Fe), apatite (P), celestine (S), and nickel oxide (Ni) were used as standards for mineral analyses.

To avoid the effects of porosity during microprobe analyses, the Si and S concentrations were calculated from the bulk composition obtained by microprobe (average of 135 defocused beam analyses; Meteoritical Bulletin Database, 2020) correlated with the ICP-AES data for Mg, Al, and Ca.

For the analyses of carbonates the following standards were used: Dolomite (Mg), jadeite (Na), calcite (Ca), strontianite (Sr), Cr_2O_3 (Cr), siderite (Fe) rhodonite (Mn), and witherite (Ba).

For quantitative (EDS) analysis using the Münster-SEM, both, samples and appropriate mineral standards were measured at an excitation voltage of 20 kV, and the beam current constancy was controlled by a Faraday cup. Standard (Astimex) olivine (Mg, Fe, Si), jadeite (Na), plagioclase (Al), sanidine (K), diopside (Ca), rutile (Ti), chromium-oxide (Cr), rhodonite (Mn), and pentlandite (Ni) were used as natural and synthetic standards. The INCA analytical program provided by Oxford Instruments was used for these EDS analyses.

FIB- and TEM-studies

FIB work was done at FSU Jena using a FEI Quanta 3D FEG FIB-SEM workstation and followed the FIB sample preparation outlined by Harries and Zolensky (2016). The TEM study of the extracted FIB sections was done at FSU Jena using a FEI Tecnai G2 FEG operated at

200 kV and equipped with an Oxford X-Max 80T SDD EDS detector and a Gatan Quantum GIF energy filter for electron energy loss spectroscopy (EELS).

FIB sampling sites were primarily selected to target sulfide crystals and adjacent phyllosilicates and locations were optimized to include other minerals of interest. A total of three FIB sections (F01-03) were extracted from thin section PL19173 of Flensburg. For comparison, two FIB sections of the Kaidun CM1 lithology in thin section 56.01 studied by Harries and Zolensky (2016) were revisited.

Computed tomography (CT)

The CT was performed at the Helmholtz-Institute Freiberg for Resource Technology. The meteorite was scanned in a CoreTom CT scanner from Tescan at 130 keV using one 0.4 mm thick steel filter mounted at the source. The current was 11 W, which is optimized so that the resolution is limited by geometrical factors and not by the spot size of the beam. The voxel size was 11.7 µm. Reconstruction was done using the XRE recon v1.0.0.111. A ring filter and a beam hardening correction of 0.45 were used to homogenize the grey-scale throughout the sample. Image processing and visualization was done in Avizo 9.3.0. A 3D non-local-means filter (window = 15, neighbour = 3, similarity = 0.4) was used to remove noise with minimum impact on object boundaries.

Modal analysis by X-ray techniques

The mineralogy of Flensburg was initially characterized using a PANalytical X'Pert Pro scanning X-ray diffractometer (XRD) at the Natural History Museum (NHM), London. For this ~1 mg of powdered sample was mixed with several drops of acetone and deposited as a thin smear on a zero-background substrate. XRD patterns were collected using Co Kα radiation from 5 – 70° (2θ) with a step size of 0.02° and time/step of 25 seconds, giving a total measurement time of ~24 hours. Mineral phases in the samples were identified using the International Centre for Diffraction Data (ICDD) database (PDF-2).

Modal mineral abundances were determined using an Enraf-Nonius PDS120 XRD equipped with an INEL curved 120° position-sensitive-detector (PSD) in a static geometry relative to the primary X-ray beam and sample. Approximately 50 mg of powdered Flensburg was loaded into an aluminium sample well using the sharp edge of a spatula to minimise preferred crystal alignments. The X-ray beam (Cu Kα_1 radiation) was restricted to 0.24 × 2.00 mm and set at an incident angle of 3.4° to the flat top of the sample which was rotated throughout the measurement. The XRD pattern for Flensburg was collected for 4 hours, and patterns of mineral standards were acquired under exactly the same experimental conditions for 15 minutes. Mineral abundances were calculated using a profile-stripping method, whereby the XRD pattern of a mineral standard was scaled to the same measurement time as the Flensburg analysis (i.e. ×16) and then reduced in intensity by a factor to match its intensity in the XRD pattern of Flensburg. The standard pattern was subtracted to leave a residual pattern. This process was repeated for all phases identified in Flensburg until there were zero counts left in the residual and the sum of the fit factors was one. The fit factors for the mineral standards were then corrected for relative differences in X-ray absorption to give their final volume fractions in Flensburg, with detection limits on the order of 0.5 – 1 vol% (for details see King et al., 2015) and uncertainties in the abundances of 0.5 – 4.4 vol%. A pattern of Flensburg is given in Fig. S16.

Bulk chemical analyses (including water and C-analyses)

The bulk sample of about 1 g from Flensburg was crushed and homogenized and about 250 mg were used for analyses at the Institut Universitaire Européen de la Mer, Université de Bretagne Occidentale in Plouzané, France. The chemical compositions of the bulk samples were obtained from a 104 mg subsample using ICP-AES (for Al, Fe, Mn, Mg, Na, Cr, Co, and Ni) and ICP-SFMS. Details are given by Barrat et al. (2012, 2015, 2016**).** The concentration reproducibility is generally much better than 5% at the chondritic level**.**

Water analyses of three samples of the Flensburg-meteorite were performed at the Institute for Geology, Mineralogy and Geophysics, Ruhr-University Bochum using a Mitsubishi CA 200 moisturemeter. For a single analysis, about 3-5 mg of the crushed sample was heated in an HF-oven to 1000°C; the gaseous components were then conducted into the titration cell, where the water content was measured by the Karl-Fischer-method. The instrument was tested with an internal laboratory standard (5 wt.% H_2O) prior to and after the measurements. The precision of this method is 5 % relatively. Effects of terrestrial water adsorption do not play a significant role. In this study, one sample was stored at room conditions for some days prior to analysis and was not annealed to 110°C prior to analysis. The result of 9.89 wt.% water demonstrates that the samples do not react with the humidity of the air and that all obtained values are identical according to the precision of the machine.

The determination of the CO_2 content was done using the C/S 500 instrument of ELTRA with an IR-detector. A sample of 13 mg was heated in an oxygen atmosphere up to 1100 °C. All carbon present reacts to form CO_2 which is transported in an oxygen flow towards the detector (C_{total}).

Oxygen isotopes

The oxygen isotope composition of bulk material of the Flensburg meteorite was analyzed by means of laser fluorination in combination with gas source mass spectrometry (for analytical details, see Pack et al., 2016 and Peters et al., 2020). Three individual chips were analyzed in two consecutive sessions. The $\delta^{17}O$ and $\delta^{18}O$ are reported on VSMOW scale, and the $\Delta'^{17}O$ is defined as

$$\Delta'^{17}O = 1000\, ln\left(\frac{\delta^{17}O}{1000} + 1\right) - 0.528 * 1000\, ln\left(\frac{\delta^{18}O}{1000} + 1\right) \qquad \text{(Equation 1)}$$

A $\Delta'^{17}O$ value of San Carlos olivine of –0.052‰ (average value of Pack et al., 2016; Sharp et al., 2016, and Wostbrock et al., 2020) was used to anchor $\delta^{17}O$ on VSMOW scale.

Titanium and Cr isotope analyses

Titanium and Cr isotope analyses on 20-50 mg samples of Flensburg were performed in Münster and Zürich. Analyses performed at the ETH Zürich were carried out on a single 26 mg aliquot of the powdered Flensburg meteorite. The analytical procedure is described in Bischoff et al. (2019).

Considering the Ti isotope analysis in Münster, an aliquot of ~30 mg sample powder (equivalent to ~20 µg Ti) was digested in HF-HNO_3-$HClO_4$ (2:1:0.05) on a hotplate at 180–200 °C for five days and in aqua regia (HCl-HNO_3) at 130–150 °C for another two days. Thereafter, the sample was dissolved in 12 M HNO_3, and ~65 mg H_3BO_3 were added. Ti was separated from the sample matrix via a two-stage anion exchange chromatography adapted from the previously established procedure from Zhang et al. (2011). In a first step, the sample solution was loaded onto a column prepacked with 2 ml TOGDA® anion exchange resin, where Ti was eluted in 20 ml 12 M HNO_3–1 wt.% H_2O_2. Afterwards, the Ti cut was dissolved in 2.5 ml 4 M HF and loaded onto a clean-up column filled with 0.8 ml Bio-Rad® AG1-X8 anion exchange resin, where Ti was eluted in 6 ml 9 M HCl–0.01 M HF.

Titanium isotope measurements were made in two lines using a ThermoScientific Neptune Plus MC-ICPMS (Multicollector Inductively Coupled Plasma Mass Spectrometry) in medium resolving power mode (Zhang et al., 2011). Solutions containing about 200 ppb Ti in 0.3 M HNO_3 – 0.0014 M HF were introduced through a Cetac Aridus II desolvating system, resulting in a ~3.5×10^{-10} A ion beam on ^{48}Ti. Mass bias was corrected using the exponential law and ^{49}Ti/^{47}Ti = 0.749766. The Ti isotope anomalies are reported as parts per ten thousand deviation (ε-notation) from the terrestrial OL-Ti (Millet and Dauphas, 2014) bracketing standard. The sample uncertainty is reported as the Student-t 95% confidence interval based on repeated analyses (n=13) of the sample solution on five different days. In the case of the Cr isotope analysis in Münster, Cr was collected during the first step of the two-stage anion exchange chromatography used for the separation of Ti, where Cr is eluted in 25 ml 12 M HNO_3 (+ trace H_3BO_3) together with most other matrix elements. An aliquot (equivalent to ~30 µg Cr) was taken from this solution, dried down, and redissolved in 1 ml 6 M HCl.

Afterward, Cr was separated from the sample matrix using a single-stage anion exchange chemistry for the removal of Fe (Bio-Rad® AG1-X8 anion exchange resin), followed by a two-stage cation exchange chromatography (Bio-Rad® AG50W-X8 cation exchange resin) as described by Yamakawa et al. (2009), including a four-day conversion of Cr[III]Cl_3/Cr[II]Cl_2 to Cr^{3+}.

Chromium isotope measurements were performed using a ThermoScientific Triton Plus Thermal Ionization Mass Spectrometer in static mode. The sample solution (~500 ppm Cr in 6 M HCl) was loaded on 4 filaments and each filament was measured multiple times, with total ion beam intensities of ~1.4×10^{-10} A on ^{52}Cr. Instrumental mass fractionation was corrected assuming a constant ^{50}Cr/^{52}Cr = 0.051859 and using the exponential law. The data is reported as ε^{54}Cr value as the parts per ten thousand deviation from the terrestrial NIST SRM3112a Cr standard. The sample uncertainty is reported as the Student-t 95% confidence interval based on repeated analyses (n=12).

Tellurium isotope analysis

The sample powder of Flensburg (~70 mg) was spiked with a ^{123}Te-^{125}Te double spike, digested in HF–HNO_3, and Te was purified using a three-stage column chemistry modified after Fehr et al. (2004) and Brennecka et al. (2017). The Te isotope measurements were performed using a Neptune *Plus* MC-ICPMS at Münster combined with a Cetac Aridus II. Results are reported in $\delta^{128/126}$Te as the per mil deviation from the NIST SRM 3156 Te standard.

Oxygen, carbon, and Mn-Cr isotope studies by SIMS

Oxygen 3 isotope, simultaneous carbon and oxygen, as well as Mn-Cr isotope compositions in calcite and dolomite were determined using the Cameca IMS1280-HR ion microprobe at Heidelberg University (HIP).

For oxygen 3 isotope measurements (Fig. 12) we used a ~ 1.3 nA, 20 keV Cs^+ primary ion beam with a raster size of 6 µm (8 µm during pre-sputtering). Negative secondary ions were accelerated to 10 keV. The secondary ion image was limited to 15 µm, the dynamic transfer optical system (DTOS) was activated and sample charging was compensated with the electron gun (NEG). ^{16}O, ^{17}O and ^{18}O were detected simultaneously in three Faraday cup (FC) detectors. The nominal mass resolving power for ^{16}O and ^{18}O was 2500 and 7000 for ^{17}O. The contribution of $^{16}OH^-$ on the ^{17}O peak was negligible at < 0.1‰. Secondary intensities for ^{16}O and ^{17}O were $\sim 1.5 \times 10^9$ cps and $\sim 6 \times 10^5$ cps, respectively. Prior to each analysis, the secondary beam was centered automatically in the field aperture (X and Y) and the entrance slit (X only). Including the time for beam centering, the analyses started after a total pre-sputtering time of 90 s and each analysis had 25 cycles with 8 s integration time per cycle. The internal precision reported is the standard deviation of the mean value of the isotope ratios. The baseline of the Faraday cup amplifiers was determined separately with an integration time of 200 s several times per session.

NBS19 limestone (NIST RM 8544, $\delta^{18}O_{VSMOW} = +28.65$ ‰, Brand et al. 2014) was used as reference material for the calibration of the oxygen isotope analyses. For $\delta^{17}O_{VSMOW}$ we assumed a value of +14.85 ‰ which was calculated using the mean $\Delta^{17}O$ value from Passey et al. (2014) and Barkan et al. (2015). The reference material was on a separate sample holder and was analyzed prior to and during the analytical session. The repeatability (1sd) for $\delta^{17}O$, $\delta^{18}O$ and $\Delta^{17}O$ of the calibration was 0.25 ‰, 0.16 ‰ and 0.26 ‰, respectively.

The dolomite O isotope analyses were corrected for the differences in instrumental mass fractionation (bias) between NBS19 (calcite) and dolomite–ankerite. A constant calcite–dolomite bias of –4.4 ‰ for $\delta^{18}O$ was assumed (Tyra et al., 2016). The dolomites have a mean Fe# of 0.10 ± 0.02 which causes an additional bias of ~ +5.8 ‰ for $\delta^{18}O$. This bias was calculated individually for each dolomite grain using the fit curve equation in Fig. 2 of Śliwiński et al. (2016a) and the Fe# calculated from the EPMA analysis of the same grain. Both bias corrections (which almost cancel each other out) were applied and the bias correction for $\delta^{17}O$ was calculated by applying a factor of 0.528 to the $\delta^{18}O$ bias correction.

For single-spot simultaneous carbon and oxygen isotope analyses, a modified setup was used: the 20 keV Cs^+ primary ion beam was reduced to 0.5 nA beam current and a raster size of 5 µm (7 µm during pre-sputtering). ^{12}C and ^{13}C (and $^{12}CH_2$ for monitoring purposes) were detected simultaneously in a FC detector (L'2) and two electron multiplier (EM) detectors (axial EM and H2), with mass resolving powers of 2500, 4000 and 2500, respectively, and typical secondary ion intensities of ~ 4×10^6 cps and ~ 4×10^4 cps, respectively. ^{16}O and ^{18}O were detected simultaneously in two FC detectors (C and H'2) with typical secondary ion intensities of ~ 7×10^8 cps and ~ 1.4×10^6 cps. This method of alternating carbon and oxygen multicollection enabled combined (and therefore correlated) carbon and oxygen isotope analyses on relatively small carbonate grains. Pre-sputtering time was 120 s and each analysis comprised 20 cycles with 15 s integration time per cycle for carbon and 8s for oxygen. Only measurements with $^{12}CH_2/^{12}C < 10^{-4}$ were used, to ensure that possible contributions from epoxy and/or organic carbon were avoided. For the oxygen isotope analyses the same standard and bias correction procedures as above were applied. For carbon isotopes measurements, again NBS19 limestone (NIST RM 8544, $\delta^{13}C_{VPDB} = +1.95$ ‰; Brand et al., 2014) was used as reference material for calibration. A constant calcite–dolomite bias of –9.2 ‰ for $\delta^{18}O$ was assumed (Tyra et al., 2016). The dolomites analyzed in this session had a mean Fe# of 0.10 ± 0.02 which caused an additional mean bias of ~ –2.6 ‰ for $\delta^{13}C$. Again, this bias was calculated individually for each dolomite grain using the fit curve equation in Fig. 2 of Śliwiński et al. (2016b) and the Fe# calculated from the EPMA analysis of the same grain. The reference material was on a separate sample holder and was analyzed prior to and during the analytical session, and the repeatability (1sd) of the calibration was 0.5 ‰ for both $\delta^{13}C$ and $\delta^{18}O$. The inevitable drift of the measured $^{13}C/^{12}C$ ratio caused by aging of the EM was corrected for by linear regression.

For Mn-Cr we used a ~ 4 nA, 23 keV O^- primary ion beam with a diameter of ~ 10 µm. Positive secondary ions were accelerated to 10 keV and the secondary ion image was limited to 15 µm. All isotopes were detected simultaneously in multi-collection mode. The nominal mass resolving power was 7000 for ^{55}Mn and 8000 for ^{52}Cr and ^{53}Cr. ^{52}Cr and ^{53}Cr were detected by electron multipliers in pulse counting mode, while ^{55}Mn was detected by the axial Faraday cup detector (10^{11} Ω amplifier) for dolomite or by the axial electron multiplier for calcite. Prior to each analysis, the secondary beam was centered automatically in the field aperture (X and Y) and the entrance slit (X only). Including the time for beam centering, the analyses started after a total pre-sputtering time of 120 s and each analysis typically consisted of 100 cycles with 4 s integration time per cycle. The $^{53}Cr/^{52}Cr$ and the $^{55}Mn/^{52}Cr$ ratios were calculated using the cumulated count rates of the isotopes. Errors of the ratios and Pearson's correlation coefficient ρ were calculated from the standard error of the mean count rates. IsoplotR (Vermeesch, 2018) was used for the linear regression (model: maximum likelihood) of the Mn-Cr isochrone.

The instrumental mass fractionation of –8 ± 1 ‰ for $^{53}Cr/^{52}Cr$ was determined using San Carlos olivine and assuming its $^{53}Cr/^{52}Cr$ ratio to be 0.11339 (Meija et al., 2013). The ion yield of Mn relative to Cr for calcite (*RIY*, defined as SIMS ratio / real ratio) was determined on the synthetic calcite MnCr–22 (Donohue et al., 2019) using concentrations next to the SIMS spots determined by EPMA. $RIY_{\mathrm{Mn/Cr,cal}}$ from 9 analyses was 0.693 ± 0.056 (1sd). Based on our $RIY_{\mathrm{Mn/Cr,\ cal}}$, we calculated our $RIY_{\mathrm{Mn/Cr,dol}} = 1.087$ using the relative sensitivity factors (which are the inverse of our *RIY*) for calcite and dolomite from Steele et al. (2017).

Analyses of bulk H, C and N elemental and isotopic compositions

The determination of the bulk H, C and N elemental and isotopic compositions of Flensburg followed the protocols used by Alexander et al. (2012, 2013). Briefly, two aliquots (~2 mg) of the crushed Flensburg sample were weighed into Ag capsules for H analysis, and two aliquots (~8 mg) were weighed into Sn capsules for C and N analysis. The samples were stored in a desiccator for several days and reweighed to remove adsorbed atmospheric water. Prior to H analysis, the samples were placed in an autosampler and flushed with zero-grade, dry He for two hours to remove water that was adsorbed from the atmosphere during the transfer from the desiccator to the autosampler.

The elemental and isotopic analyses were made with: 1) a Thermo Scientific DeltaV$^{\mathrm{plus}}$ mass spectrometer connected to a Carlo Erba (NA 2500) elemental analyzer (CE/EA) via a Conflo III interface for C and N analyses, and 2) a Thermo Finnigan Delta$^{\mathrm{plus}}$XL mass spectrometer connected to a Thermo Finnigan Thermal Conversion elemental analyzer (TC/EA) via a Conflo III interface for H analyses. The Conflo III interface facilitates the introduction of the N_2 and CO_2 reference gases for the N and C isotope analyses. in contrast a dual inlet system facilitates the introduction of the H_2 reference gas for the H isotope analyses. A H_3^+ correction was determined and applied to the H measurements (Sessions et al., 2001). We used in-house standards to normalize and correct the data at regular intervals to monitor the accuracy and precision of the measured isotopic ratios and elemental compositions throughout the runs. These in-house standards, which included both gases and solid materials, have been calibrated against international (SMOW, NBS-22, PDB, and air) and other certified standards from Isoanalytical, USGS, NBS and Oztech. Standards were analyzed at regular intervals to monitor the internal precision of the measured isotopic ratios and elemental compositions throughout the run. The reported uncertainties for the elemental and isotopic analyses correspond to the highest 1σ deviations attained from either the replicate analyses of distinct subsamples ($n > 2$) or the internal standards.

For the H analyses, the two samples were analyzed sequentially to check for both sample heterogeneity and small memory effects that are known to occur. Blanks were also run before and after them, again to reduce any memory effects. There was little evidence for significant heterogeneity or memory effects. There is no memory effect for C and N analyses.

Radionuclides

Radionuclide analysis by non-destructive low-level gamma-spectrometry was performed in the underground laboratory “Felsenkeller” in Dresden, Germany (Niese et al., 1998). The laboratory is situated under a rock overburden of 138 m w.e. (water equivalent), resulting in a suppression of the total muon intensity by a factor of 30-40 (Ludwig et al., 2019). A gamma-spectrometry system dedicated to the analysis of very low activity levels was utilized. The spectrometer is based on a coaxial p-type high-purity germanium (HPGe) detector of 92% relative efficiency with enhanced front-side sensitivity for low-energy gamma-rays. All construction elements were selected for low radioactivity contents. The passive shielding is graded and consists of 5 cm of electrolytic copper, 5 cm of low-activity lead (2.7 Bq kg^{-1} ^{210}Pb) and an outer layer of 10 cm lead with 33 Bq kg^{-1} ^{210}Pb. Detailed information about the gamma-spectrometry system can be found in Köhler et al. (2009).

The non-destructive gamma-spectrometric measurement of the whole specimen (24.5 g) started on 11th October 2019 (less than one month after the bolide event) and was continued until 28th October with some short breaks (<1 h) due to device maintenances, resulting in a total measurement time of 17 days. To allow for a more precise radionuclide determination, the energy-dependent detection efficiency of the detector was determined from the measurement of a meteorite dummy made of material with known naturally-occurring radionuclide contents.

For the destructive determination of long-lived radionuclides via accelerator mass spectrometry (AMS), a 35.60 mg aliquot of the homogenized bulk powder (~1 g) was radiochemically treated (Merchel and Herpers, 1999). It yielded in the production of suitable chemical compounds BeO, Al_2O_3, AgCl, CaF_2, NiO, MnO_2, and Fe_2O_3. Basic steps were: (a) addition of stable isotope carriers (^{9}Be, ^{27}Al, ^{nat}Cl, ^{nat}Ca, ^{55}Mn) in the form of solutions; (b) pressurized digestion in HF/HNO_3; (c) liquid aliquot for ICP-MS measurements for determination of natural occurring Al, Ca, Fe, Mg, Mn, and Ni; (d) anion and cation exchange; (e) precipitations; (f) drying and partial oxidation for oxide compounds and (g) mixing with metal powder, i.e., BeO with Nb, all other oxides and CaF_2 with Ag. To date these target materials have been analyzed for cosmogenic radionuclides ^{10}Be, ^{26}Al, ^{41}Ca, and ^{60}Fe by AMS. Measurements of the remaining other nuclides are foreseen in the future (^{36}Cl, ^{53}Mn, ^{59}Ni). The Flensburg sample was chemically treated together with six other ordinary chondrites and a corresponding processing blank. The latter sample combines all sources from the background, i.e. from chemical processing and AMS measurements (Table S9), and is of utmost importance for samples with radionuclide contents near the detection limit. A separate sample (25 mg) was extracted at the University of Arizona, and the ^{14}C measurement was made at the Arizona AMS Laboratory, using procedures described in Jull et al. (1998).

The heavier nuclides (^{41}Ca and ^{60}Fe) were determined at the Heavy Ion Accelerator Facility (HIAF) at the Australian National University (ANU) in Canberra (Wallner et al., 2015, 2016), whereas the lighter nuclides were measured at the 6 MV AMS-facility DREAMS in Dresden (Akhmadaliev et al., 2013; Rugel et al., 2016). In-house AMS-standards and calibration materials used are SMD-Be-12 with $^{10}Be/^{9}Be = (1.704 \pm 0.030) \times 10^{-12}$, SMD-Al-11 with $^{26}Al/^{27}Al = (9.66 \pm 0.14) \times 10^{-12}$, SMD-Ca-11 with $^{41}Ca/^{40}Ca = (9.944 \pm 0.092) \times 10^{-12}$, and in-house ^{60}Fe/Fe material (known to ~10%), which is based on material provided by the TU Munich and on material from recent meteorite studies (Leya et al., 2020). They had been previously cross-calibrated against material from PSI with a well-known ^{60}Fe/Fe ratio of $(1.234 \pm 0.007) \times 10^{-12}$ (Schumann et al., 2019). All calibration materials are half-life independent. However, for the conversion of isotope ratios into specific radionuclide activities, we have used the following half-life values: (1.387 ± 0.012) Ma for ^{10}Be (Korschinek et al., 2010), (0.705 ± 0.024) Ma for ^{26}Al (Norris et al., 1983), and (0.104 ± 0.005) Ma for ^{41}Ca (Paul et al., 1991) to compare with production rates (see below).

Specific activities are compared to time-, depth-, and radius-depending production rates from theoretical Monte Carlo calculations (Leya and Masarik, 2009). These are based on input parameters for target elements from ICP-SFMS measurements (Table 4) for Ca, Ti, Mn, Rb, Sr, Y, Zr, Ba; from ICP-MS measurements from the liquid aliquot of the AMS sample for Fe, Mg, Ni; and from Table 5 for C and N. Data for important target elements producing lighter radionuclides, i.e. Na, Al, Si, and S, have been taken from microprobe analysis. The water content has been taken into account by filling–up all measured element concentrations to 99% with oxygen, i.e., leaving 1% for hydrogen (from H_2O), which is producing no relevant radionuclides. In the current version of the calculation tool kindly provided by Ingo Leya (U Bern) no adjustment for different densities are easily possible, which influences the precision of shielding depths and radii.

IR Spectroscopy

For the mid-infrared reflectance spectroscopy, a Bruker Vertex 70v spectrometer in the IRIS lab at the Institut für Planetologie of the University of Münster was used. Polished thin sections of Flensburg (PL19171) and of other meteorites were analyzed (Table S8). Possible organic contamination at the surface of the thin sections was removed with ethanol. We used different observation geometries for the measurements with the incident and emergent angle between 20° and 40°, using a Bruker A513 bidirectional reflectance stage. The used detector was a liquid nitrogen cooled MCT-detector. The mean of 512 interferogram scans per geometry was calculated in the measured wavelength range from 2 to 18 µm. All measurements took place at room temperature of ~23°C and at pressures of ~2 hPa. For the background calibration, we use a polished gold mirror. The spectral data will be available in the upcoming IRIS database for space science missions (Weber et al., 2018).

Organics

Twelve T Fourier transform ion cyclotron mass spectrometry (FTICR/MS) and 800 MHz ^1H nuclear magnetic resonance spectroscopy (NMR) based characterization used methanolic extracts obtained from the solid specimen with a weight of a very few mg as developed for characterization of Murchison and other extraterrestrial soluble organic matter (SOM) (Schmitt-Kopplin et al., 2010; Popova et al., 2013; Hertkorn et al., 2015). A single fragment of Flensburg (20.6 mg) was divided into several aliquots; two pieces (~5 mg each) were washed with LC/MS grade methanol (Fluka) to remove surface contamination; this washing fluid was discarded. Both fragments were consecutively crushed and ground in an agate mortar with an agate pestle for ~20 sec under LCMS grade methanol. The solutions were transferred to two separate Eppendorf tubes and centrifuged at 16000 rpm for 3 minutes. The first solution was directly used for FTICR mass spectrometry (Schmitt-Kopplin et al., 2010). For NMR spectroscopy, the centrifugate was transferred to a glass flask and evacuated in a vacuum (with loss of unspecified volatiles). Then, 750 µL CD_3OD (99.95% ^{2}H, Merck) were added, followed by vacuum evaporation. This procedure was repeated two times to fully exchange CH_3OH with CD_3OD. Prior to all operations, all vessels and handling devices were extensively washed with LCMS grade methanol to attenuate terrestrial contamination as far as possible. A ^{1}H NMR spectrum, with solvent suppression (*noesypr1d*) was acquired with a Bruker AV III 800 spectrometer operating at B_0 = 18.7 T, as described in Hertkorn et al. (2015), from 45 µL extract in 1.7 mm Bruker NMR Match tubes, with number of scans = 22194 and processed with an exponential line broadening of 4 Hz. ^{1}H NMR spectra of CD_3OD alone (~450 µL; ns = 1392) were acquired under identical conditions, and did not show NMR resonances obtained from Flensburg SOM at any relevant S/N ratio (data not shown in Figures of this work).

Magnetic Properties

The magnetic properties of the rock were studied in Aix-en-Provence and Nördlingen. Most magnetic measurements were performed at CEREGE (Aix-en-Provence, France) on a 267 mg bulk sample with no fusion crust. Hysteresis measurements were performed with a Princeton Micromag Vibrating Sample Magnetometer (VSM) with a maximum applied field of 1 T and a sensitivity of ~$5x10^{-9}$ Am^2. The analysis of hysteresis loops provided the ratio of saturation remanent magnetization (M_{RS}) to saturation magnetization (M_S) and the coercive force (B_C). High field susceptibility (χ_{HF}) was determined by a linear fit for applied fields > 0.9 T of the hysteresis loops. Remanent coercive force (B_{CR}) was determined by back field experiments performed with the VSM. The low field specific susceptibility (χ in m^3/kg) and its evolution at low temperature were measured using Agico MFK1 apparatus with sensitivity of $5x10^{-13}$ m^3, operating at 200 A/m and a frequency of 976 Hz, equipped with a CSL cryostat. The coercivity spectrum was estimated through stepwise acquisition and measurement of isothermal remanent magnetization (IRM) using the VSM. We determined the S_{-300} ratio, defined as the IRM obtained after applying a 3 T field and then a back field of 0.3 T normalized to the IRM acquired in 3 T. For this experiment, IRM was imparted using a pulse magnetizer from Magnetic

Measurement. Remanence measurements were performed with a 2G SQUID magnetometer model 755R) equipped with an automatic 3-axis alternating field (AF) demagnetization system. In Nördlingen, the Magnetic Susceptibility (MS) was measured with the handheld device SM-30 from ZH Instruments (www.zhinstruments.cz).

Density

The density of Flensburg was measured by two different methods: In a first approach, the bulk density of the rough piece was determined in Augsburg with the method described by Consolmagno et al. (1998) using 40 µm diameter glass beads. In a later measurement the volume of the 17.03 g piece obtained by CT was used for density calculations. Consistent results were obtained by both methods.

Parent body modeling

The thermal evolution of the Flensburg parent body was calculated using a 1D thermal evolution code (Neumann and Kruse, 2019; Neumann et al., 2020) that was adapted to a carbonaceous chondritic composition specific to the Flensburg meteorite. The code uses a finite-differences grid and solves conservation equation for energy as well as equations for the evolution of porosity that result in a global contraction of the body considered. The model accounts for heating by short- and long-lived radionuclides (Table S10) and for the consumption of the latent heat of water ice melting. The pre-hydration initial composition included a water mass fraction of 10%, producing a post-hydration phyllosilicate mass fraction of 84%. The model incorporates an initial microporosity of 0.5. Compaction of the porous material was calculated (Neumann et al., 2014, 2015, 2020) using experimentally determined creep laws, i.e., a power law for phyllosilicates (Hilairet et al., 2007; Amiguet et al., 2012) and a diffusion creep equation for the remaining fraction of the material (Schwenn and Goetze, 1978). An initial and ambient temperature of 170 K was adopted as appropriate for water-rich objects that were accreted outside of the snow line (Hayashi, 1981). For the choice of temperature- and porosity-dependent material properties according to a phyllosilicate-rich composition and for a detailed model description, we refer to Neumann et al. (2020).

Table S1: Representative analyses of calcite (Calc), dolomite (Dol), and the Na-rich carbonate (Na-carb.); All data are in wt.%. n.d. = not detected.

	Calc	**Calc**	**Calc**	**Calc**	**Dol**	**Dol**	**Dol**	**Dol**	**Na-carb**
MgO	0.06	0.19	<0.02	0.05	16.4	16.3	16.2	15.6	0.05
Na_2O	n.d.	<0-03	n.d.	<0.03	0.06	0.04	0.08	n.d.	12.3
CaO	56.7	56.7	56.6	56.0	30.1	29.0	29.4	30.4	44.0
SrO	0.14	0.08	n.d.	n.d.	0.06	<0.02	<0.02	n.d.	0.06
Cr_2O_3	<0.02	n.d.	0.07	n.d.	0.06	0.09	<0.03	n.d.	n.d.
FeO	0.43	0.82	0.91	0.75	3.6	4.0	3.6	3.6	0.51
MnO	0.65	0.21	0.10	0.06	3.5	3.7	3.9	3.8	n.d.
BaO	0.06	<0.03	0.08	n.d.	<0.03	0.05	n.d.	n.d.	n.d.

Table S2: Representative analyses of sulfides in Flensburg. Pentlandite = Pent; pyrrhotite = Po; all data are in wt.%; n.d. = not detected.

	S	**Fe**	**Co**	**Ni**	**Total**
Pent	33.4	33.2	1.61	30.9	99.2
Pent	33.9	37.7	1.34	27.0	100.0
Pent	33.1	33.5	1.49	31.6	99.6
Pent	32.3	39.8	1.23	24.9	98.2
Pent	33.9	42.4	1.10	21.0	98.4
Pent	33.4	34.6	1.38	31.6	100.9
Po	38.5	61.2	n.d.	0.57	100.3
Po	38.5	61.4	n.d.	0.18	100.0
Po	38.5	61.3	n.d.	0.38	100.2
Po	38.1	61.6	n.d.	0.23	99.9
Po	38.8	61.0	n.d.	0.56	100.3
Po	37.8	61.5	n.d.	0.18	99.6

Table S3: Representative analyses of oxides in Flensburg. Mag = magnetite; Chr = chromite. All data in wt.%. n.d. = not detected; oxygen of magnetite analyzed and not calculated. Oxygen of chromite calculated assuming all Fe being Fe^{2+} (TEM-EDX, totals normalized to 100 wt.%).

	O	**Mg**	**Si**	**Fe**	**Ti**	**Cr**	**Mn**	**Ni**	**Total**
Mag	27.1	0.17	2.12	67.9	0.37	0.06	0.13	<0.04	97.9
Mag	26.8	0.06	2.06	68.3	0.09	0.07	0.07	0.05	97.6
Mag	27.9	0.06	2.09	67.9	0.58	0.05	0.13	<0.04	98.8
Mag	27.9	0.06	1.67	69.0	0.08	0.09	0.10	<0.02	99.0
Mag	27.1	0.14	1.87	68.1	0.20	0.06	0.15	n.d.	97.8
Mag	26.8	0.06	2.10	68.2	0.07	0.05	0.14	<0.04	97.5
Mag	27.0	0.07	1.59	69.6	n.d.	n.d.	0.13	0.10	98.6
Mag	26.6	n.d.	0.04	71.7	n.d.	n.d.	<0.03	0.06	98.5
Mag	27.3	0.04	2.02	68.7	0.17	0.08	0.04	n.d.	98.4
	O	**Mg**	**Al**	**Fe**	**Ti**	**Cr**	**Mn**	**Ni**	**Total**
Chr	33.3	4.8	10.5	22.4	4.2	24.7	<0.10	n.d.	100
Chr	33.9	5.1	12.4	21.0	3.1	24.6	<0.10	n.d.	100

Table S4: Simultaneous single-spot carbon and oxygen isotope data of Flensburg calcites and dolomites. Uncertainties are 1 sigma (1s), dolomite errors do not contain uncertainties of systematic correction for calcite–dolomite bias (Tyra et al., 2016) and uncertainties of correction for Fe content (Śliwiński et al. 2016a,b) for δ^{13}C and δ^{18}O.

Calcite

analyses	**δ^{13}C**	**1s**	**δ^{18}O**	**1s**
CO@0	+34.0	0.6	+17.3	0.3
CO@1	+41.4	0.3	+23.4	0.3
CO@2	+46.5	0.5	+18.0	0.3
CO@6	+40.4	0.3	+19.2	0.3
CO@9	+47.0	0.3	+24.2	0.2
CO@10	+45.5	0.5	+16.7	0.3
CO@11	+60.4	0.4	+16.0	0.4
CO@15	+24.0	0.3	+16.6	0.3
CO@16	+37.1	0.2	+16.1	0.3
CO@17	+63.5	0.4	+16.1	0.4
CO@20	+23.7	0.6	+15.2	0.3
CO@22	+33.1	0.6	+16.4	0.5
CO@24	+41.7	0.4	+16.5	0.3
CO@25	+53.2	0.4	+16.8	0.3
CO@26	+47.3	0.3	+17.4	0.2
CO@30	+24.9	1.3	+19.2	0.6
CO@34	+37.2	0.5	+21.0	0.5
CO@39	+51.3	0.4	+15.1	0.2
CO@43	+45.9	0.5	+15.0	0.3
CO@46	+45.0	0.2	+14.9	0.2
CO@47	+43.8	1.9	+17.1	0.2
CO@48	+28.4	1.1	+20.5	0.2
CO@49	+51.1	0.5	+31.0	0.3
CO@50	+50.0	0.5	+18.3	0.3
CO@54	+25.5	0.9	+17.5	0.3
CO@57	+44.4	0.4	+14.8	0.4
CO@58	+45.0	0.3	+15.0	0.3
CO@62	+44.9	0.4	+14.6	0.4
CO@63	+46.2	0.4	+15.1	0.4
CO@64	+44.1	0.3	+16.5	0.7
CO@67	+43.3	0.3	+24.9	0.4
CO@71	+45.4	0.3	+14.9	0.3
CO@74	+46.1	0.4	+19.0	0.3
CO@75	+59.6	0.5	+14.8	0.3
CO@76	+28.1	0.3	+17.5	0.2
CO@78	+42.3	0.5	+26.7	0.2
CO@79	+39.6	0.5	+17.4	0.2
CO@86	+47.9	0.3	+16.7	0.2
CO@90	+41.0	0.3	+21.8	0.3
CO@92	+41.6	1.1	+25.4	0.3
CO@94	+16.3	0.4	+16.8	0.4
CO@96	+35.2	0.4	+15.9	0.2
CO@97	+26.0	1.0	+17.0	0.2
CO@99	+45.2	0.4	+15.4	0.3
CO@100	+16.8	0.4	+14.9	0.4
CO@102	+43.8	0.4	+25.3	0.4
CO@106	+41.9	0.5	+23.5	0.3
CO@107	+43.9	0.4	+25.2	0.4
CO@108	+45.2	0.5	+14.5	0.3
Calcite continued				
CO@109	+48.3	0.4	+13.6	0.2
CO@110	+45.1	0.3	+14.7	0.3
CO@112	+45.6	0.4	+19.5	0.4
CO@113	+36.4	0.8	+14.3	0.3
CO@114	+39.5	0.5	+18.1	0.6
CO@120	+43.5	0.4	+16.3	0.3
CO@121	+49.7	0.5	+15.2	0.4
CO@122	+18.5	0.5	+16.0	0.3
CO@124	+51.8	0.5	+15.6	0.4
CO@130	+28.3	1.1	+15.7	0.3
CO@131	+32.4	1.6	+21.2	0.5
CO@134	+46.4	0.3	+16.7	0.3
CO@135	+20.7	0.9	+22.0	0.2

Dolomite

analyses	**δ^{13}C**	**1s**	**δ^{18}O**	**1s**
CO@7	+55.2	0.3	+14.9	0.3
CO@8	+57.7	0.3	+13.0	0.4
CO@12	+58.8	0.4	+14.8	0.3
CO@13	+55.3	0.4	+14.8	0.3
CO@21	+48.7	0.5	+12.7	0.4
CO@23	+48.6	0.6	+13.0	0.5
CO@24	+52.9	0.4	+16.7	0.3
CO@27	+57.4	0.4	+15.2	0.3
CO@29	+49.1	0.3	+13.4	0.2
CO@33	+54.7	0.3	+13.8	0.3
CO@37	+57.2	0.9	+15.3	0.3
CO@53	+58.7	0.3	+15.1	0.3
CO@56	+55.5	0.4	+15.5	0.3
CO@59	+59.8	0.5	+15.3	0.4
CO@60	+53.8	2.3	+15.6	0.3
CO@61	+49.1	0.3	+13.4	0.3
CO@65	+59.4	0.3	+16.4	0.4
CO@69	+59.5	0.3	+14.7	0.3
CO@72	+59.2	0.3	+15.7	0.2
CO@73	+56.7	0.3	+14.3	0.3
CO@77	+55.5	0.5	+14.9	0.3
CO@87	+50.8	0.6	+14.1	0.3
CO@88	+58.7	0.4	+15.2	0.3
CO@89	+58.0	0.3	+15.6	0.2
CO@95	+58.1	0.3	+16.4	0.2
CO@101	+54.8	0.9	+16.5	0.2
CO@105	+59.0	0.4	+15.2	0.3
CO@111	+57.4	0.3	+14.4	0.4
CO@116	+58.7	0.3	+16.3	0.2
CO@118	+57.6	0.3	+15.7	0.3
CO@123	+58.5	0.4	+16.0	0.2
CO@133	+49.1	0.3	+14.8	0.3

Table S5a: Results of analyzed EMPA and SIMS spots. The location of the spots (denoted with @) can be found in Fig. S17). RIY= Relative Ion Yield; SE = Standard Error

EPMA No.	**Cr (wt%)**	**Mn (wt%)**	**^{55}Mn/^{52}Cr**	**SIMS-Nr. @**	**^{55}Mn/^{52}Cr**	**1SE (%)**	**RIY**
6	0.330	0.996	3.411				
25	0.333	0.793	2.688				
26	0.315	0.915	3.283				
	0.326	0.901	3.124	**HIGP@0**	2.383	0.862	0.763
13	0.318	1.258	4.465				
21	0.355	1.223	3.890				
23	0.313	0.864	3.119				
26	0.315	0.915	3.283				
	0.325	1.065	3.698	**HIGP@1**	2.354	0.259	0.636
9	0.285	0.713	2.828				
10	0.323	0.761	2.663				
12	0.349	0.897	2.903				
18	0.278	0.913	3.704				
19	0.162	0.768	5.352				
	0.279	0.810	3.276	**HIGP@2**	2.090	0.563	0.638
16	0.151	0.495	3.697				
17	0.273	0.819	3.390				
33	0.276	0.909	3.715				
34	0.175	0.525	3.386				
	0.219	0.687	3.545	**HIGP@3**	2.313	0.524	0.653
12	0.349	0.897	2.903				
13	0.318	1.258	4.465				
18	0.278	0.913	3.704				
22	0.272	1.061	4.412				
	0.304	1.032	3.831	**HIGP@4**	2.729	0.539	0.712
1	0.304	0.822	3.058				
4	0.318	0.925	3.283				
11	0.341	0.798	2.639				
	0.321	0.848	2.984	**HIGP@5**	2.365	0.652	0.793
2	0.291	0.637	2.476				
3	0.325	0.693	2.409				
8	0.290	0.661	2.572				
	0.302	0.664	2.483	**HIGP@6**	1.768	0.453	0.712
35	0.318	1.294	4.595				
36	0.304	0.868	3.228				
37	0.285	0.795	3.146				
38	0.298	0.980	3.721				
	0.301	0.984	3.691	**HIGP@7**	2.477	0.327	0.671
27	0.332	0.960	3.269				
30	0.323	0.917	3.207				
	0.327	0.939	3.239	**HIGP@8**	2.140	0.407	0.661
						mean RIY:	**0.693**
						1sd:	**0.056**

Table S5b: ^{55}Mn/^{52}Cr and ^{53}Cr/^{52}Cr values for calcites and dolomites within the unique Flensburg carbonaceous chondrite; SE = Standard Error; rho = correlation coefficient ρ

Calcite

^{55}Mn/^{52}Cr	**1SE**	**^{53}Cr/^{52}Cr**	**1SE**	**rho**
0.6	0.0	0.11285	0.00023	0.27
77**e**.5	4.9	0.11259	0.00952	0.63
3.7	0.1	0.11303	0.00311	0.59
81773.4	4008.9	0.44256	0.04037	0.53
475977.9	62142.1	2.01613	0.30784	0.85
385629.2	45422.3	1.87962	0.26333	0.83
10735.1	981.5	0.16362	0.01987	0.73
1764.1	49.1	0.12078	0.00478	0.69
22371.1	1463.3	0.21880	0.03285	0.43
12240.3	898.4	0.19548	0.03244	0.43
697.4	17.1	0.10730	0.00445	0.51
1239.5	91.0	0.11934	0.01100	0.44
2.9	0.2	0.11316	0.01254	0.68
22.0	0.6	0.11207	0.00342	0.56
112768.2	7540.5	0.57808	0.06387	0.60
263002.2	26135.2	1.64956	0.20663	0.78
2.9	0.1	0.11288	0.00507	0.68
31.7	1.5	0.11260	0.00772	0.69
6564.0	1175.9	0.14706	0.03462	0.75
223220.7	27505.5	1.17892	0.19233	0.74
95.1	1.7	0.11336	0.00272	0.66
2.8	0.0	0.11294	0.00108	0.47
3.0	0.0	0.11278	0.00159	0.55
1172.8	15.2	0.11911	0.00288	0.49
30.3	0.8	0.11197	0.00341	0.60
8.3	0.4	0.11286	0.00584	0.56
40.3	0.7	0.11311	0.00269	0.70

Table S5b
continued

Dolomite

$^{55}Mn/^{52}Cr$	1SE	$^{53}Cr/^{52}Cr$	1SE	rho
2261.0	116.1	0.12028	0.00830	0.73
1010.3	70.8	0.11622	0.01126	0.72
842.2	108.8	0.11582	0.02076	0.71
139844.3	3746.9	0.76061	0.03342	0.59
560894.7	32598.4	2.83122	0.18740	0.87
2097.9	161.4	0.11994	0.01257	0.73
129.8	7.3	0.11321	0.00890	0.71
5417.2	596.2	0.13471	0.01941	0.76
1024.5	10.9	0.11691	0.00183	0.56
415790.0	18865.9	2.03796	0.10974	0.83
2904.1	105.8	0.12659	0.00621	0.72
37534.1	2128.4	0.25751	0.01726	0.84
686397.0	51568.0	3.15657	0.25311	0.93
11392.0	764.0	0.15398	0.01292	0.79
732501.0	43705.5	3.81986	0.25636	0.88
27278.0	710.8	0.24055	0.00861	0.71
59425.8	3876.4	0.36707	0.02693	0.88
519781.6	31107.1	2.78918	0.19056	0.87
1850871.8	165943.6	8.56855	0.81712	0.93
376.5	6.4	0.11441	0.00263	0.69
793568.2	59502.5	3.79338	0.31196	0.90
506955.1	26619.2	2.56623	0.15556	0.86
782467.6	41007.2	3.64626	0.22111	0.85
2971.9	163.4	0.12373	0.00916	0.73
655883.1	36649.8	3.11253	0.19758	0.87
111920.2	6335.3	0.63070	0.03988	0.89
7879.8	401.3	0.14567	0.01012	0.72
1048.8	64.8	0.11615	0.00986	0.72
1478.8	42.7	0.11862	0.00478	0.70
5.8	0.1	0.11289	0.00093	0.45
1031334.2	74678.0	4.93189	0.38447	0.92
184440.4	5517.1	0.89266	0.03892	0.67
419413.6	18920.6	1.90747	0.10126	0.84
15358.9	378.2	0.16736	0.00594	0.67
346.4	6.7	0.11482	0.00309	0.70
624794.7	33451.2	2.89495	0.17537	0.87
452181.2	20582.8	2.14644	0.11778	0.82
682229.5	33766.3	3.11895	0.17450	0.87
292984.1	11313.0	1.30304	0.06241	0.79
243083.2	9155.5	1.21331	0.05793	0.77
372088.9	15207.4	1.83029	0.09195	0.80
2516.0	194.2	0.12043	0.01245	0.74
825291.9	40436.2	3.51696	0.19645	0.87
120605.0	2747.4	0.66094	0.02348	0.62

Table S6: Range of possible production rates $P_{x,}$ determined for radii <200 cm and allowed shielding depths based on a $^{22}Ne/^{21}Ne$ ratio of 1.11 and bulk chemistry given in Table 4 using the model of Leya and Masarik (2009) for noble gases ^{38}Ar, ^{21}Ne, and ^{3}He.

$cm^3/(g×Ma)$	**P_{38}**	**P_{21}**	**P_3**
All allowed shielding depths	0.030-0.047	0.130-0.304	1.166-1.899
Restricted shielding depths*	0.030-0.047	0.145-0.304	1.177-1.898

*production rates restricted to most probable shielding depths, assuming 85% mass loss during atmospheric entry, excluding 22% of the inner radius excluding thereby 1 % of the mass (see text for details).

Table S7: Maximum cosmic ray exposure ages T_x in Ma based on restricted production rates of noble gases ^{38}Ar, ^{21}Ne, and ^{3}He.

	T_{38}	**T_{21}**	**T_3**	**CRE age range**
S	0.39±0.13	0.17±0.10	0.25±0.09	0-0.20±0.05
L	0.20±0.06	0.14±0.08	0.20±0.07	

Table S8: Overview of the meteorites used for infrared spectroscopy, the PL-number of the used thin section, ID to the IRIS (Infrared and Raman for Interplanetary Spectroscopy) data base, aperture, and viewing geometry of the measurements.

Meteorite	Class, type, group	PL-number	ID	Aperture in mm	Viewing geometry in °	Wavelength region in µm
Flensburg	C1 ung	PL19171	198	1.5	i25;e15	8 to 18
Flensburg	C1 ung	PL19171	198	0.5	i20;e15	2 to 4
Alais	CI1	PL92322	201	0.5	i20;e30	8 to 18, 2 to 4
Orgueil	CI1	PL92321	210	0.5	i20;e15	8 to 18
Orgueil	CI1	PL92321	210	1.5	i40;e30	2 to 4
Murchison	CM2	PL89464	204	0.5	i20;e15	8 to 18
Cold Bokkeveld	CM2	PL17148	211	0.5	i20;e30	8 to 18, 2 to 4
Allende	CV3	PL04256	203	0.5	i20;e15	8 to 18
Acfer 182	CH3	PL01267	202	0.5	i20;e15	8 to 18

Table S9: AMS data for Flensburg and corresponding processing blank. ^{10}Be and ^{26}Al have been measured at Dresden, and ^{41}Ca and ^{60}Fe at Canberra. Specific activities for ^{10}Be, ^{26}Al, and ^{41}Ca for Flensburg are calculated from the AMS ratios, ICP-MS results (^{27}Al and ^{nat}Ca) or carrier addition (^{9}Be), sample weight and half-lives. The specific activity values are blank-corrected and their given uncertainties (1-sigma) include those associated to blank-corrections.

	Flensburg	Blank
^{10}Be [counts]	2108	42
^{10}Be/^{9}Be [E-15]	97.3±2.9	1.92±0.30
^{10}Be [dpm/kg]	0.0539±0.0016	
^{26}Al [counts]	151	1
^{26}Al/^{27}Al [E-15]	149±15	$1.8^{+3.2}_{-1.1}$
^{26}Al [dpm/kg]	0.209±0.030	
^{41}Ca [counts]	5	1
^{41}Ca/^{40}Ca [E-15]	23^{+16}_{-13}	$4.3^{+7.6}_{-2.8}$
^{41}Ca [dpm/kg]	$0.37^{+0.32}_{-0.26}$	
^{60}Fe [counts]	1	1
^{60}Fe/Fe [E-17]	6^{+11}_{-4}	$4.0^{+7.0}_{-2.6}$
^{60}Fe [dpm/kg]	comparable to blank	

Table S10: Parameters used for calculation in the models. The data for the calculation of the radiogenic energy production are from Barrat et al. (2012), Kita et al. (2013), Tang and Dauphas (2012), Finocchi and Gail (1997), and Van Schmus (1995). The element mass fractions refer to stable isotopes, the initial ratios are between unstable and stable isotopes of an element, and the decay energies are per particle.

Isotope	^{26}Al	^{60}Fe	^{40}K	^{232}Th	^{235}U	^{238}U
Element mass fraction	$1.16\cdot10^{-2}$	$2.12\cdot10^{-1}$	$3.42\cdot10^{-4}$	$3.98\cdot10^{-8}$	$1.12\cdot10^{-8}$	$1.12\cdot10^{-8}$
Half-life (years)	$7.17\cdot10^{5}$	$2.62\cdot10^{6}$	$1.25\cdot10^{9}$	$1.41\cdot10^{10}$	$7.04\cdot10^{8}$	$4.47\cdot10^{9}$
Initial ratio	$5.25\cdot10^{-5}$	$1.15\cdot10^{-8}$	$1.5\cdot10^{-3}$	1.0	0.24	0.76
Decay energy (J)	$4.99\cdot10^{-13}$	$4.34\cdot10^{-13}$	$1.11\cdot10^{-13}$	$6.47\cdot10^{-12}$	$7.11\cdot10^{-12}$	$7.61\cdot10^{-12}$

Figures:

Fig. S1: Map showing the daylight fireball of September 12, 2019 (yellow arrow) and the finding site of the 24.5 g Flensburg meteorite in northern Germany. The yellow points indicate the video cameras which recorded the bolide. DC: Dorian Cieloch (Wremen), CH: Christian Hirsch (Hannover-Laatzen), JS: Jörg Strunk (Herford), HS: Holger Scheele (Rügen), MM: Mertrade shipyard (Marknesse), LP: Leon Pepping (Almere Buiten), GK: Gerard Kemna (Nijmegen), WS: NV Westerscheldetunnel (Marchal van Lare). Using the calibrated video recordings of the locations JS, GK and HS, the trajectory of the fireball was calculated by Jiří Borovička and Pavel Spurný, Ondřejov. Map: Google Earth.

Fig. S2: The Flensburg stony meteorite weighing 24.5 grams in pristine finding condition. The chondrite shows black primary fusion crust, which is typical for a fresh fall, and unusual ochre-colored secondary fusion crust on some broken faces (windows) of the meteorite fragment. Photos: Erik Due-Hansen.

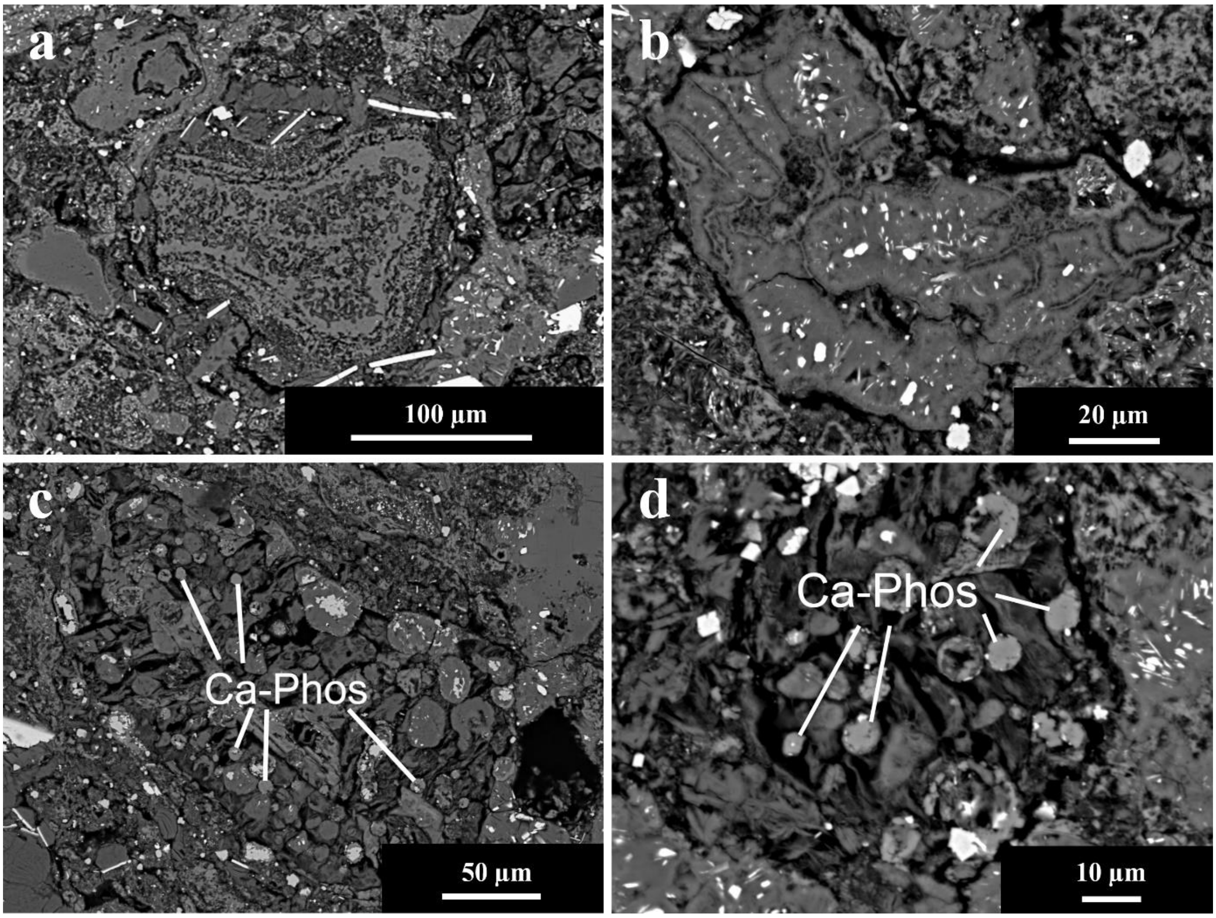

Fig. S3: (a) Irregularly-shaped object in Flensburg resembling a fragment of a CAI or AOA; (b) another irregularly-shaped, phyllosilicate-rich object embedding small sulfide grains; (c) and (d) Ca-phosphate-bearing components in Flensburg. BSE-images.

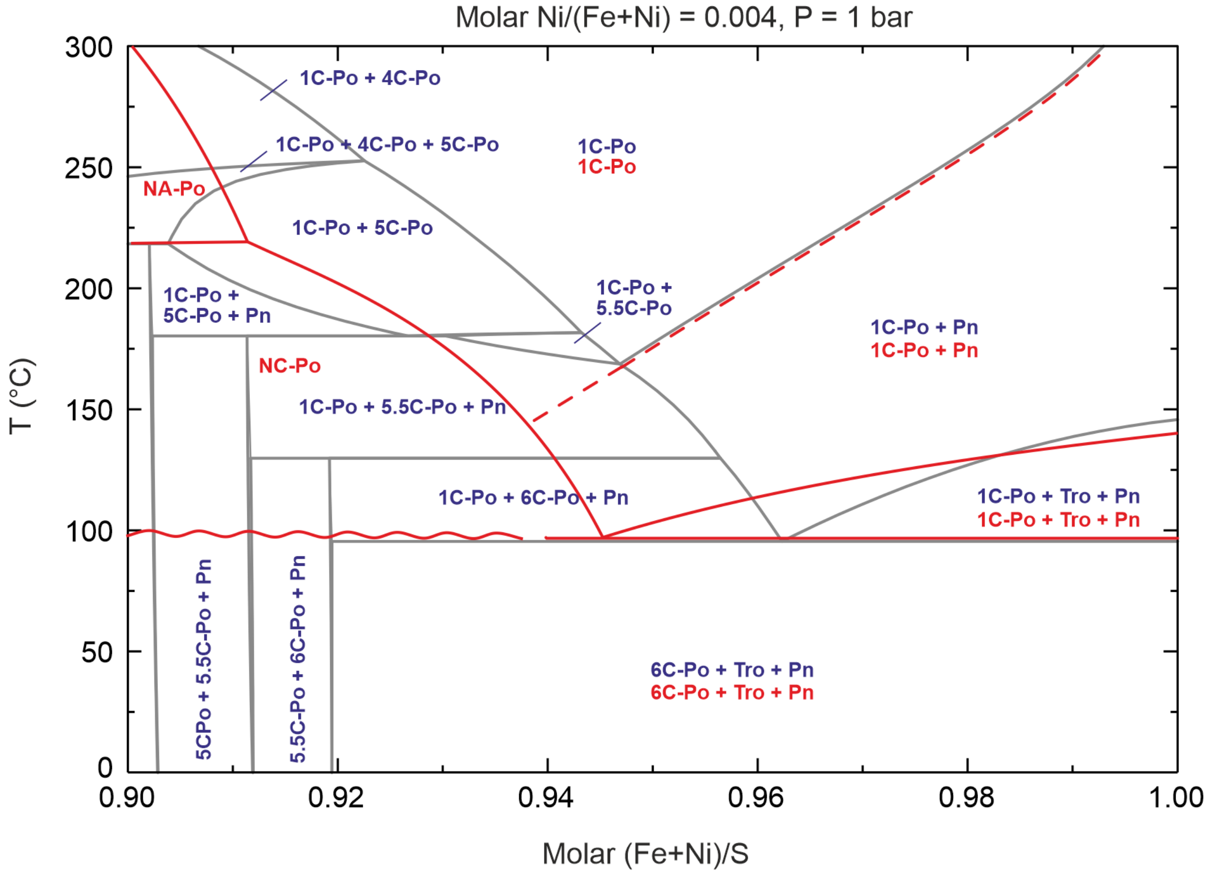

Fig. S4: TX section of the ternary Fe-Ni-S system calculated with the FactSage equilibrium solver incorporating the thermodynamic data of Waldner and Pelton (2004) and the observed mean Ni/(Fe+Ni) ratio of low-Ni iron sulfide in the Flensburg samples. Po: pyrrhotite, Pn: pentlandite, Tro: troilite. The red lines show the tentative Ni-free phase diagram of Nakazawa and Morimoto (1970) based on experimental results. It is distinct as it contains the non-integral NC- and NA-pyrrhotites, for which there are no thermodynamical data available. The use of the 5C and 5.5C (11C) variants of pyrrhotite diminish the stability field of disordered monosulfide solid solution (1C-pyrrhotite) – it is not clear whether these phases are stable or metastable against NC-pyrrhotite. Any monosulfide solid solution formed in equilibrium with pentlandite should have obtained a molar (Fe+Ni)/S ratio on the line separating the 1C-Po and 1C-Po + Pn fields (dashed line). A conservative (low) estimate of the formation temperatures of such a phase would be roughly 150 to 200 °C for intermediate metal/sulfur ratios around 0.95 – temperatures would be larger for larger metal/sulfur ratios. These would produce large amounts of exsolved troilite (>50 vol.%), which is in most cases not observed in the Flensburg low-Ni iron sulfides.

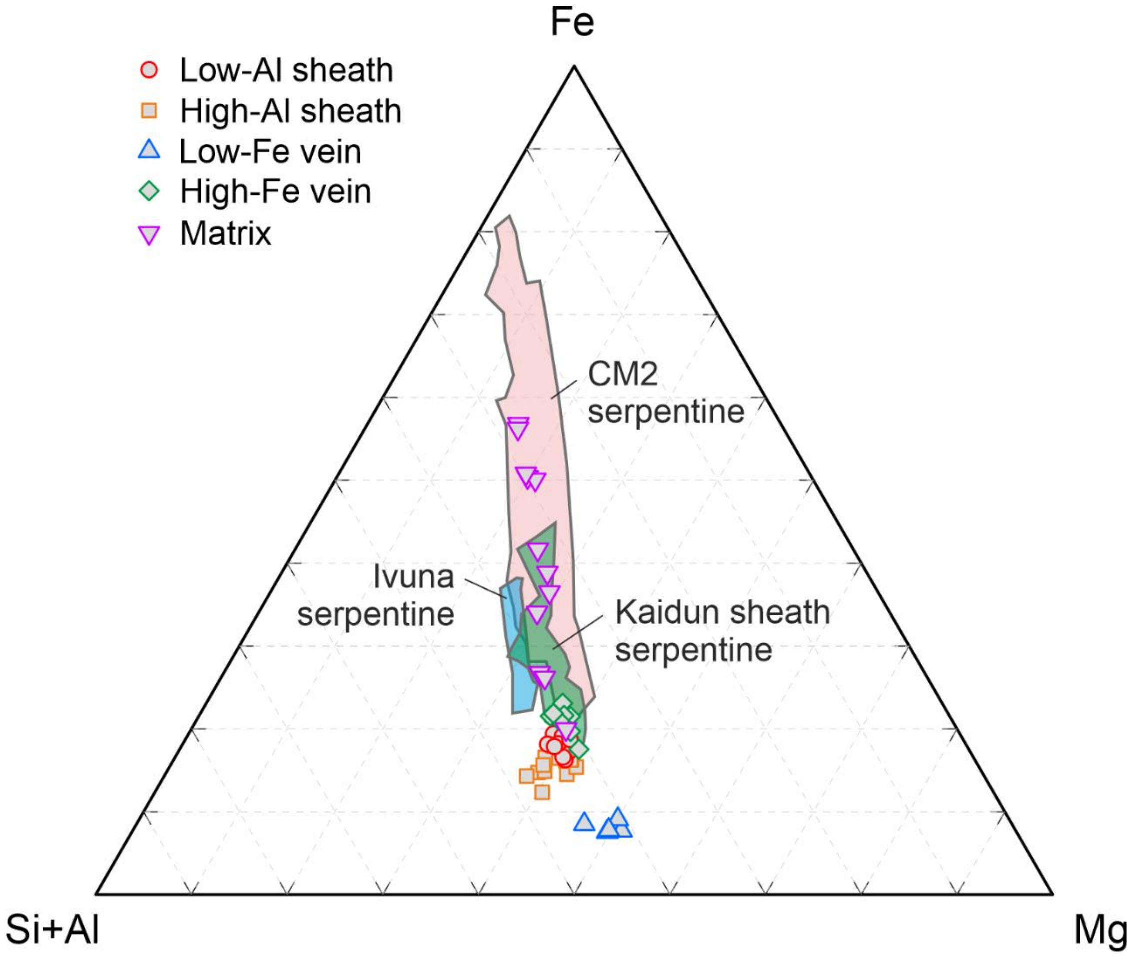

Fig. S5: TEM-EDS compositions (relative mass fractions) of serpentine in Flensburg, subdivided into sheath serpentine (covering euhedral pyrrhotite crystals), vein serpentine (occurring as short veinlets) and matrix serpentine; compare Table 2. For comparison, the fields of phyllosilicates in CM2 chondrites, Kaidun CM1 lithologies, and the Ivuna CI1 chondrite are shown (from Zolensky et al., 1996).

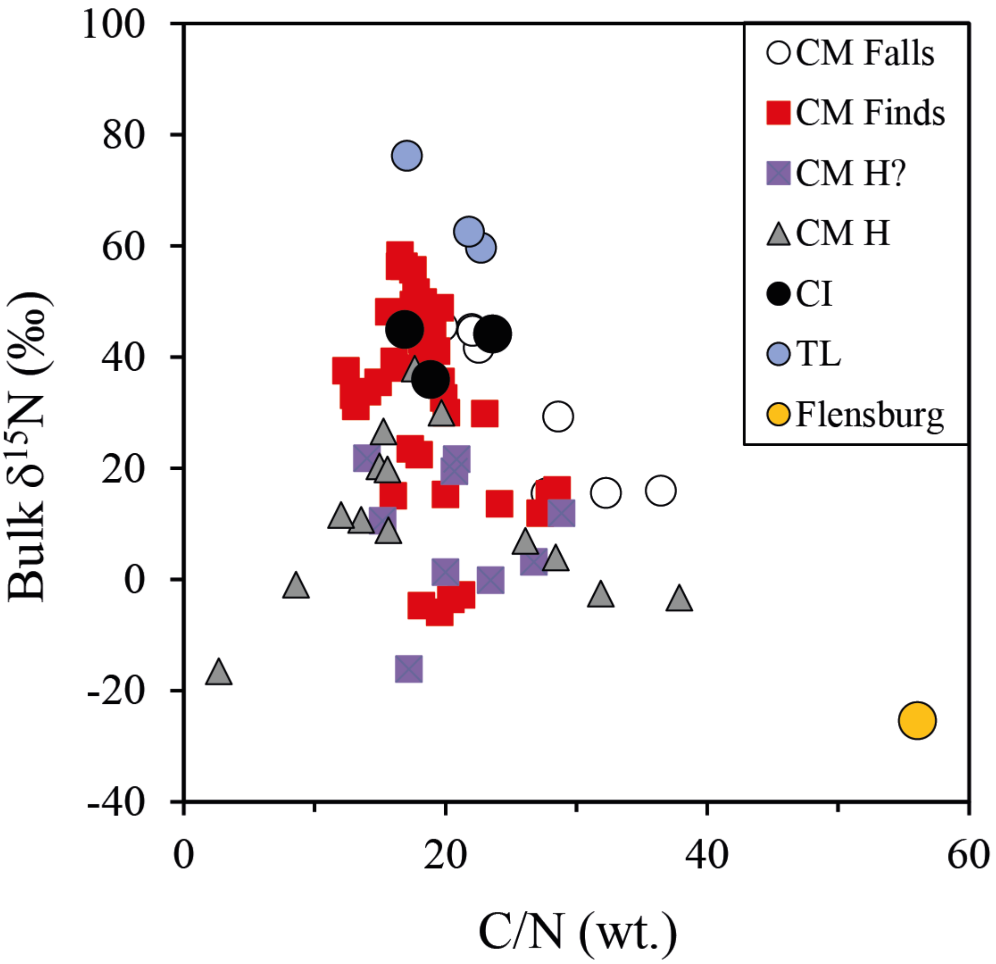

Fig. S6: Bulk δ^{15}N versus C/N-ratio of Flensburg and other type 1-2 carbonaceous chondrites (Alexander et al., 2012, 2013). Flensburg occupies a unique position in this diagram. CM H = heated CM chondrite; CM H? = possibly heated CM; TL = Tagish Lake.

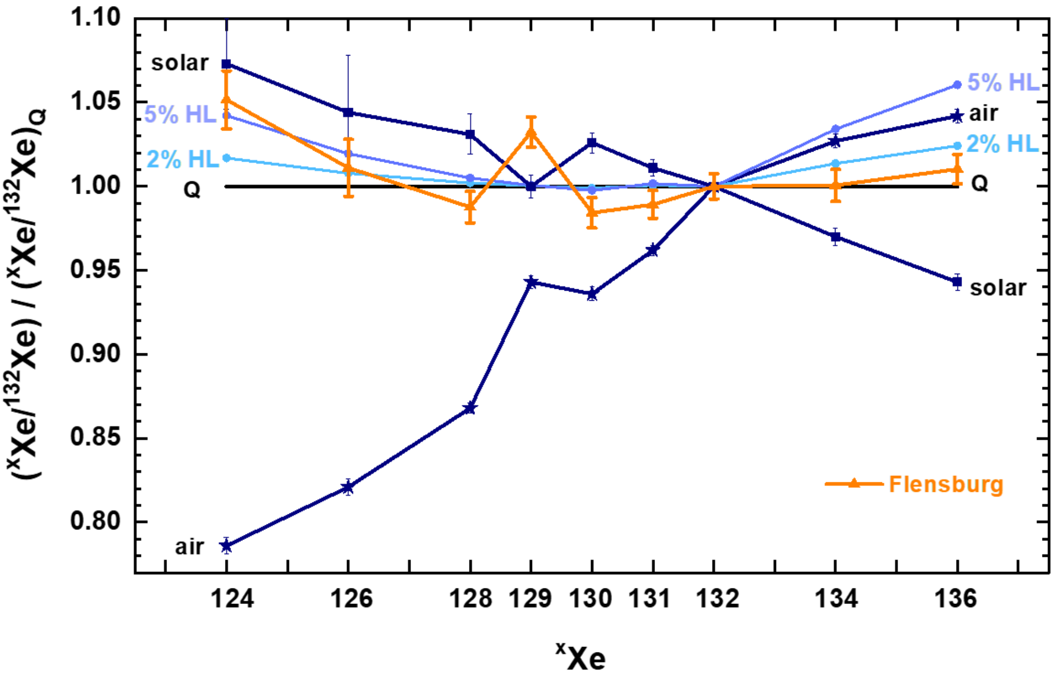

Fig. S7: ^{x}Xe/^{132}Xe normalized to Q for all relevant Xe isotopes compared to typical air and solar wind signatures. Additionally, HL-Q mixtures with 5% HL and 2% HL (based on ^{132}Xe) are plotted, showing a possible HL contribution to the signature.

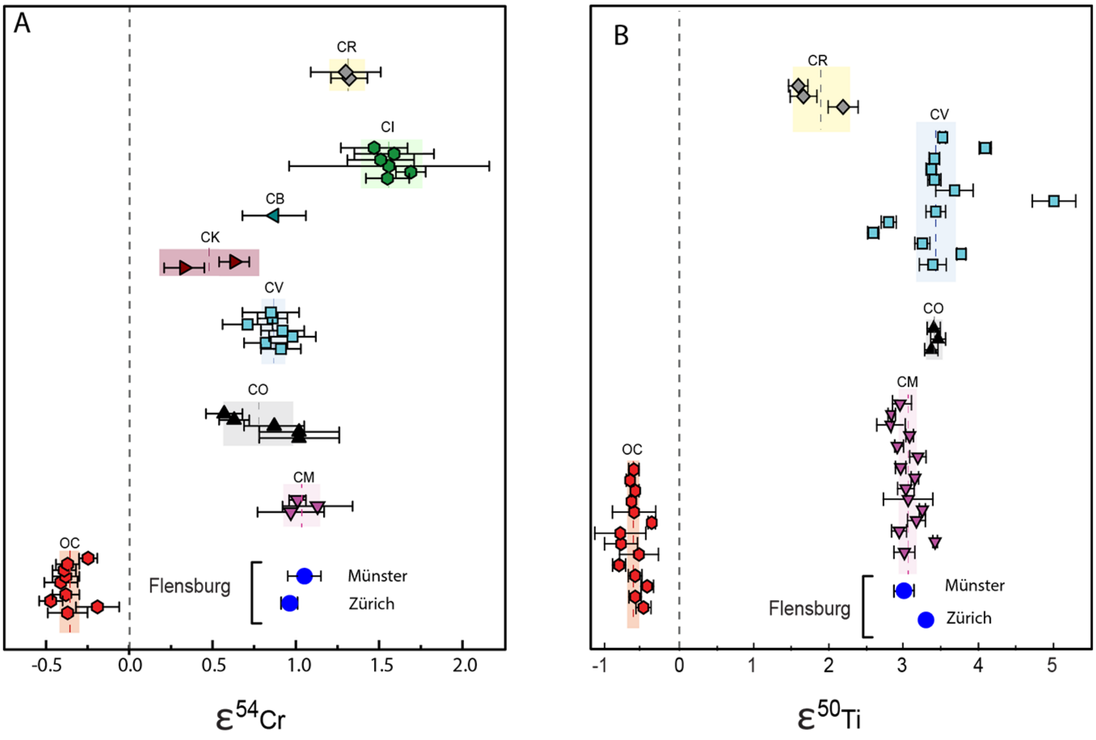

Fig. S8: (a) Chromium isotope compositions of different chondrite groups. Data are from this study, Shukolyukov and Lugmair (2006), Trinquier et al. (2008a,b), and Qin et al. (2010). (b) Titanium isotope compositions of several chondrite groups. Data from this study, Williams (2015), Trinquier et al. (2009), Zhang et al. (2011, 2012), Bischoff et al. (2017), and Burkhardt et al. (2017). Error bars and envelope in both diagrams are 2 SE.

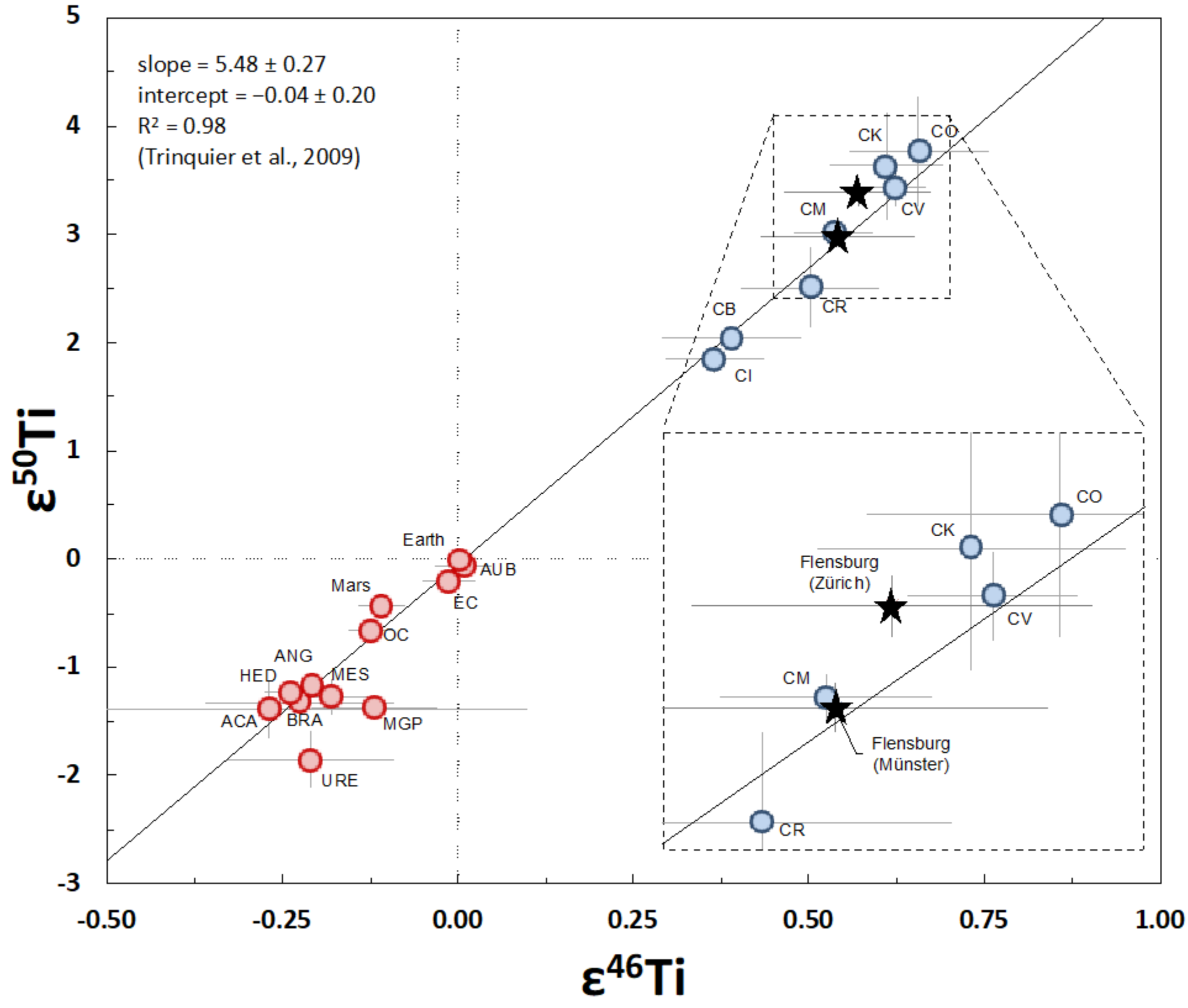

Fig. S9: ε^{46}Ti vs. ε^{50}Ti isotope diagram showing the nucleosynthetic Ti isotope composition of Flensburg (black stars) compared to literature data of various meteorite groups (red and blue circles). Uncertainties are Student-t 95% confidence interval (95% CI). The solid black line represents a best-fit regression for bulk meteorite samples, taken from Trinquier et al. (2009). EC: enstatite chondrites, OC: ordinary chondrites, AUB: aubrites, ANG: angrites, ACA: acapulcoites, BRA: brachinites, HED: howardite-eucrite-diogenite group, MGP: main group pallasites, MES: mesosiderites, URE: ureilites. Ti isotope literature data from: Trinquier et al., 2009; Zhang et al., 2011; Zhang et al., 2012; Burkhardt et al., 2017; Gerber et al., 2017; Sanborn et al., 2019; Goodrich et al., 2017.

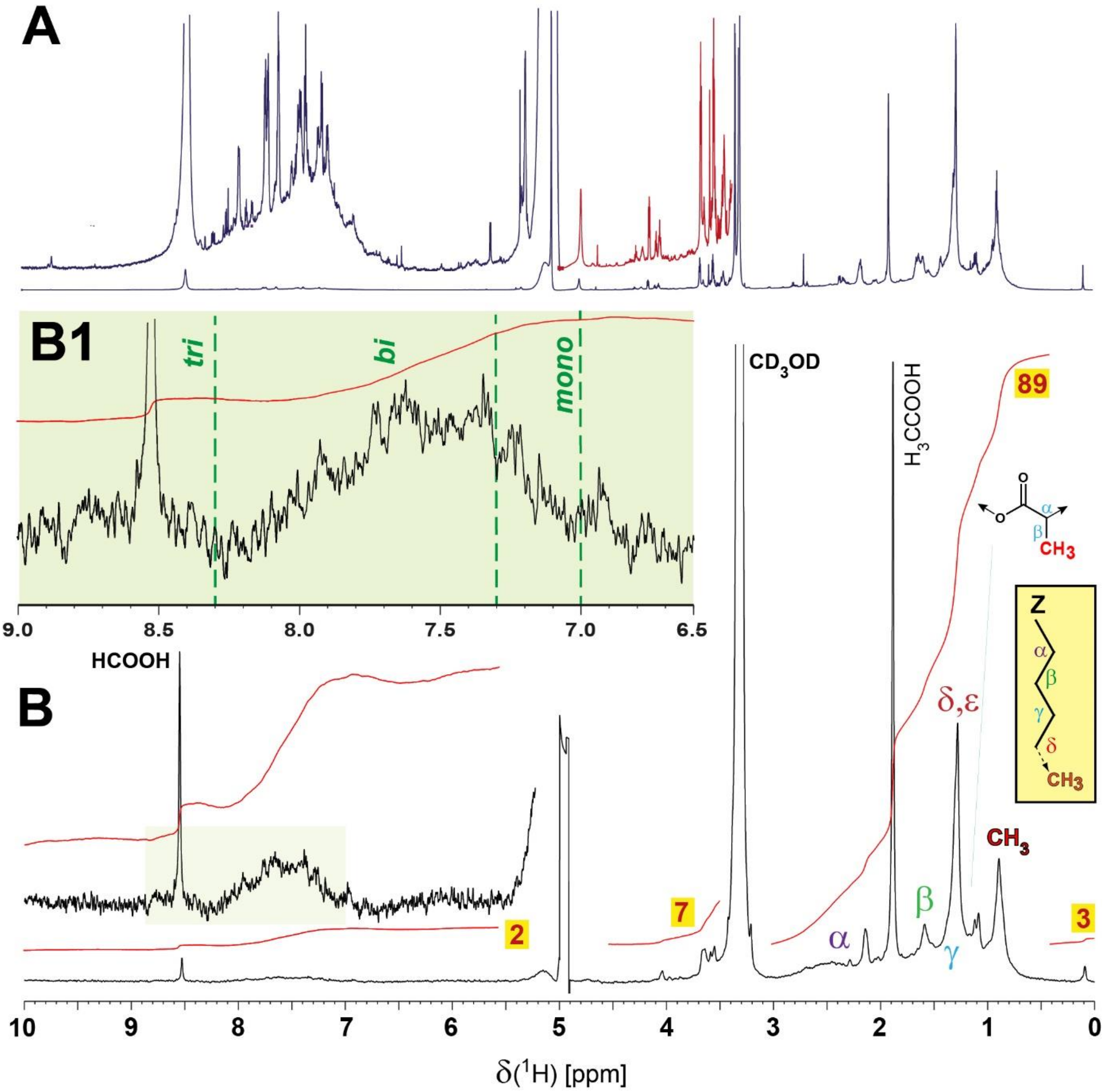

Fig. S10: The ^{1}H NMR spectra (800 MHz; CD$_3$OD, with solvent suppression) are shown of the Murchison methanolic extract (panel A; same data as in panel A7; Fig. 2, in Hertkorn et al., 2015) and the Flensburg methanolic extract (panel B). Panel B1 shows a section of aromatic ^{1}H NMR resonances $C_{ar}\underline{H}$, shaded in green (cf. also panel B) with common ranges of proton chemical shifts δ_H provided for common polycyclic aromatic rings of different size (Dvorski et al., 2016). Red numbers highlighted in yellow indicate percent ^{1}H NMR section integrals (with exclusion of methanol and water).

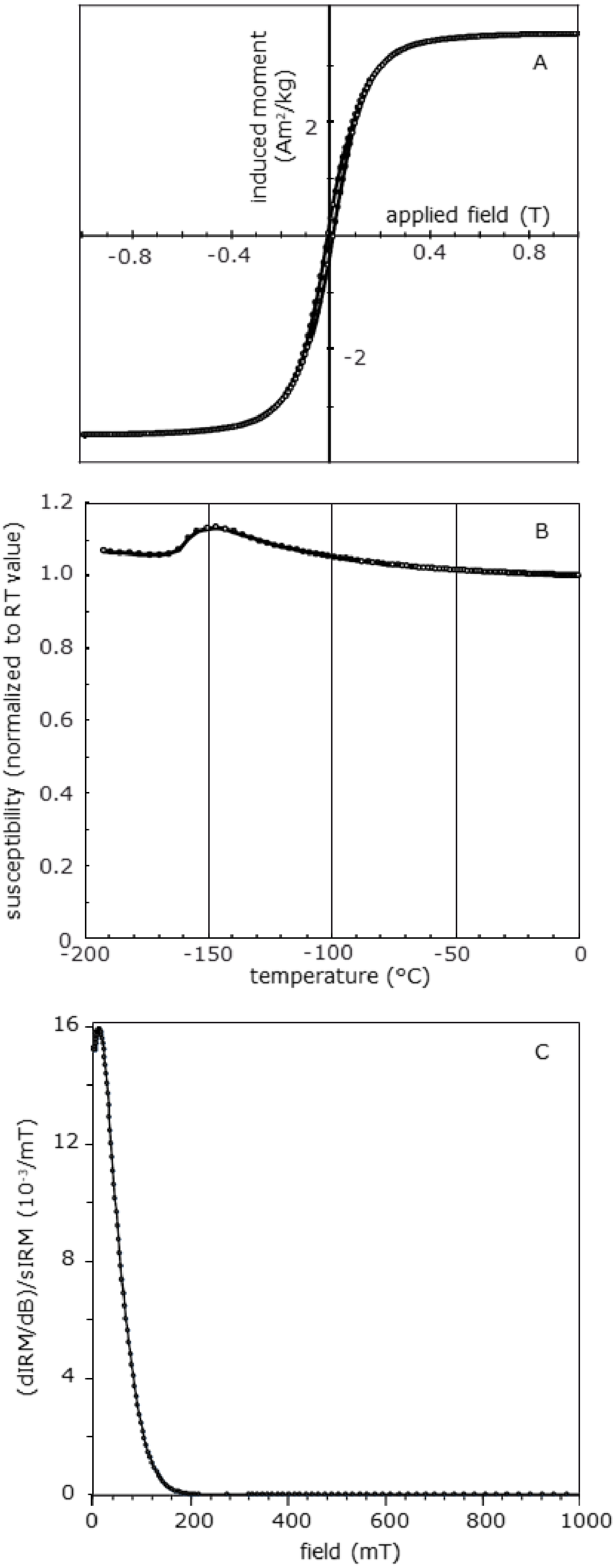

Fig. S11: All measurements were performed on the same 267 mg bulk sample without fusion crust. a) Hysteresis loop. The induced moment is corrected for the paramagnetic susceptibility computed over the 0.9-1T interval. b) Susceptibility as a function of temperature. c) Coercivity spectrum shown as the derivative of the IRM acquired as a function of acquisition field, normalized to the saturation IRM.

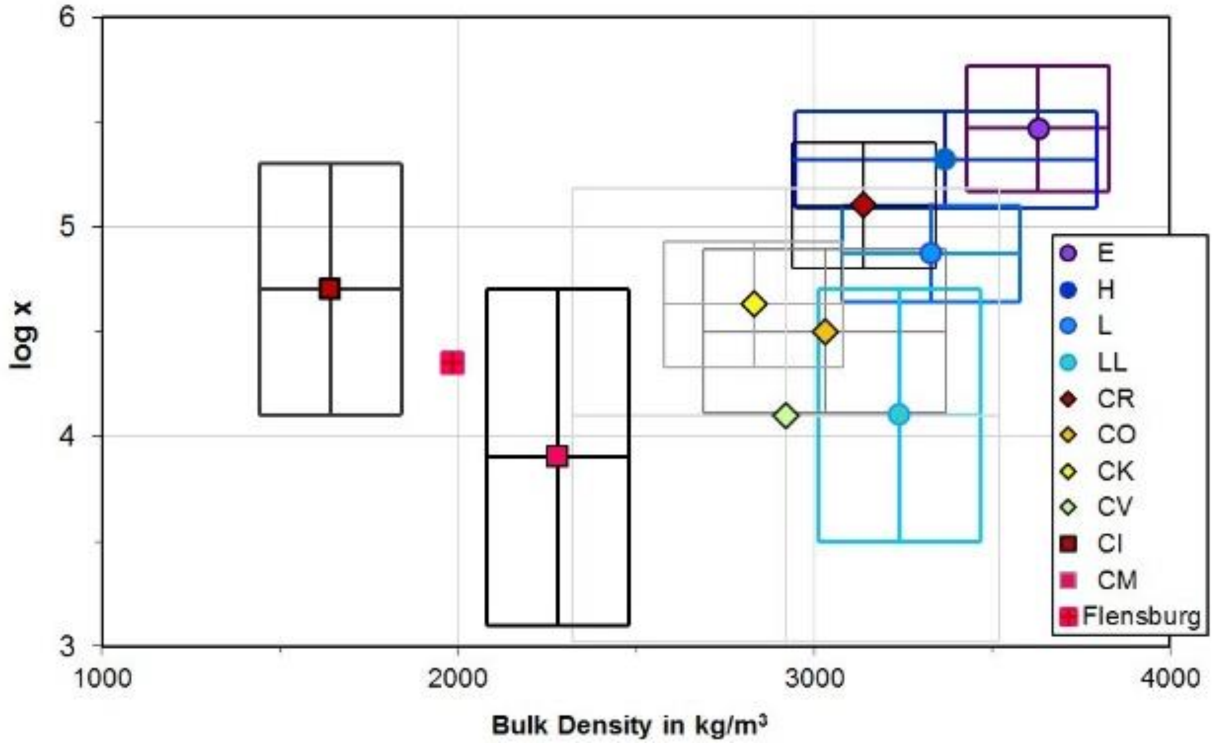

Fig. S12: Illustration of the magnetic susceptibility and density of Flensburg. Flensburg has a density plotting between the range of CI and CM chondrites.

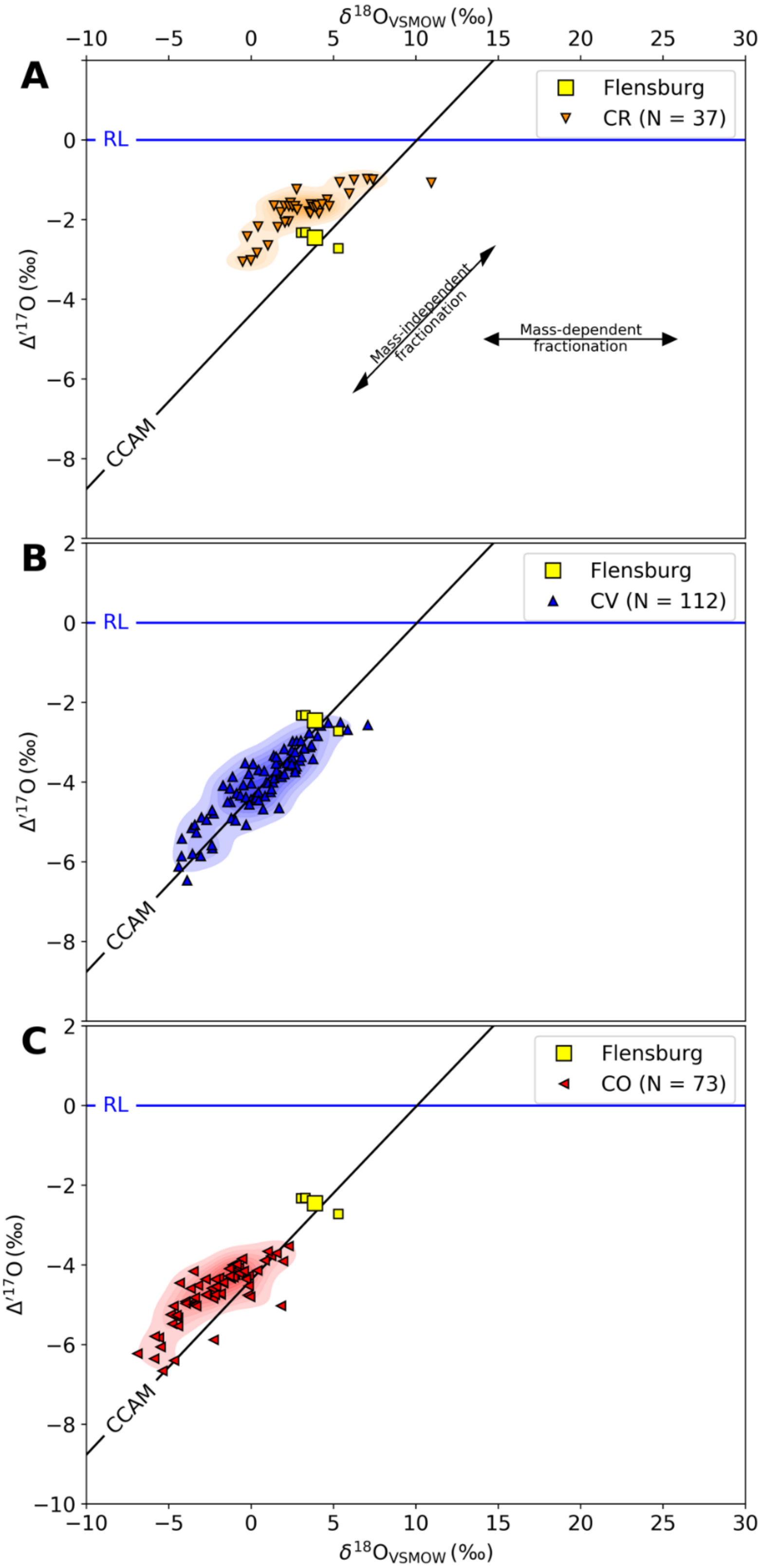

Fig. S13: Plot of the oxygen isotope composition of Flensburg in comparison to published composition of (a) CR chondrites, (b) CV chondrites, and (c) CO chondrites. The Δ'^{17}O data have been calculated using equation 1 (Supplement). The chondrite data have been obtained from the Meteoritical Bulletin database (https://www.lpi.usra.edu/meteor/, access February 2020). The carbonaceous chondrite anhydrous minerals mixing line (CCAM, $\delta^{17}O = 0.9467\ \delta^{18}O - 4.3674$) is taken from Clayton (2008). RL = reference line.

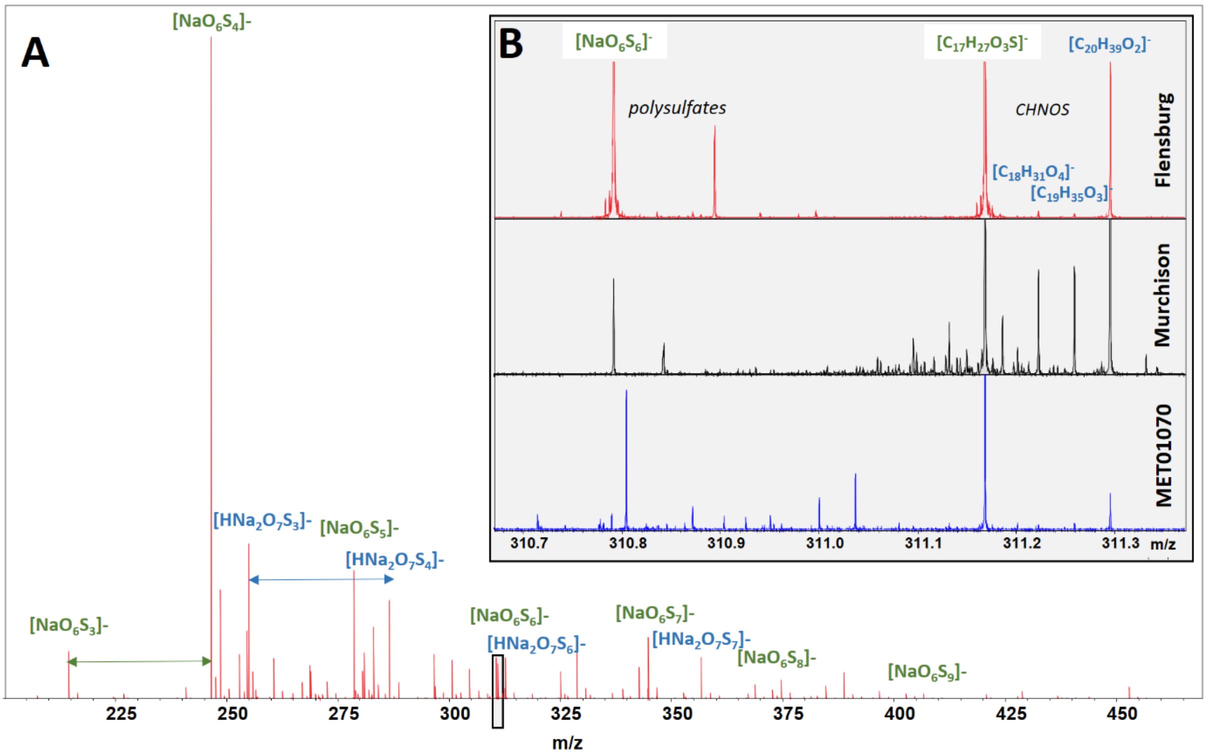

Fig. S14: Electrospray FTICR-MS spectra in the negative mode of the Flensburg methanol extract showing in panel (A), the whole mass range with subsequent intense regular signals corresponding to various polythiol species with up to 9 sulphur atoms. Panel (B) shows the detail of nominal mass 311, indicating the relatively poor chemical diversity of Flensburg compared to Murchison (CM2.5-CM6 breccia; Schmitt-Kopplin et al., 2010); both Flensburg and MET011070 (CM1) have only a few (n<10) and similar mass peaks compared to the high chemical diversity observed in Murchison (n>80).

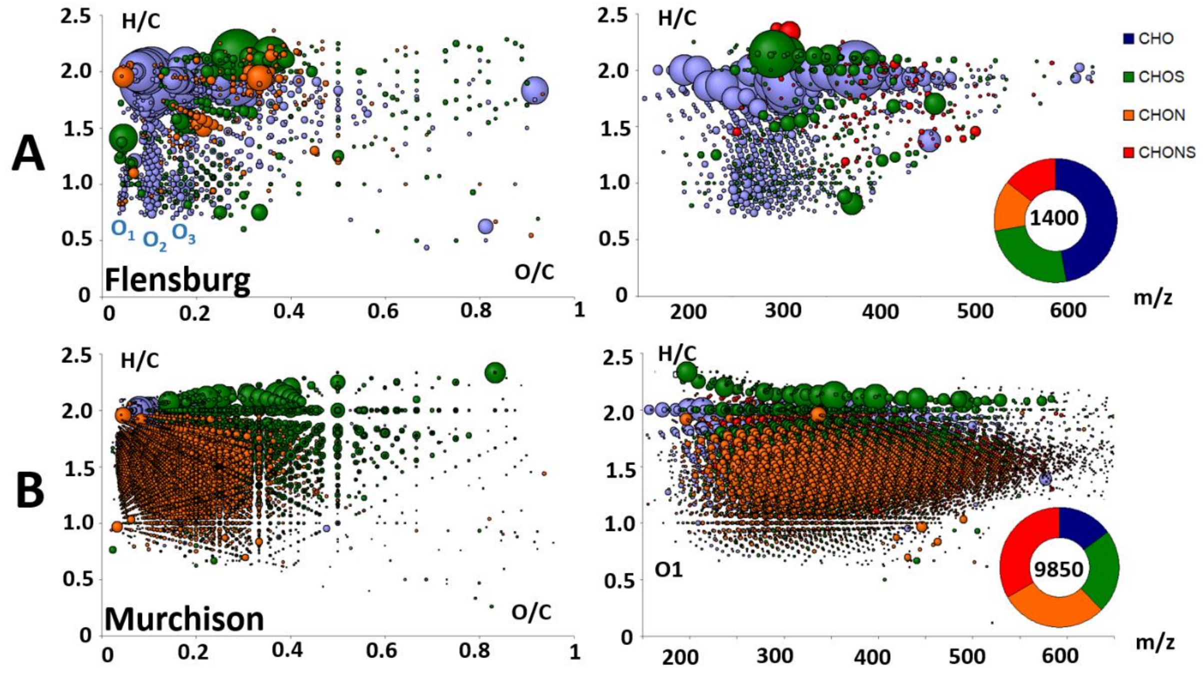

Fig. S15: Van Krevelen diagrams of the Flensburg and Murchison methanol soluble organic matter (SOM) showing the high diversity in S and N chemistry in Murchison (B) compared to Flensburg (A). For Flensburg ~1400 formula (species) are recorded, from which the CHO compounds (blue) are the most abundant, while 9850 species were found for Murchison, in which the respective molecular series decrease according to CHNOS (red) > CHNO (orange) > CHOS (green) > CHO (blue). A remarkable molecular signature of Flensburg SOM is shown representing mono-, di- and tri-oxygenated aromatic hydrocarbons (labelled O_1, O_2 and O_3), respectively), with an H/C range from 1.5 to 0.5, representative of variable extents of aliphatic groups. The bubble size expresses the relative intensity of the signals in the experimental mass spectra.

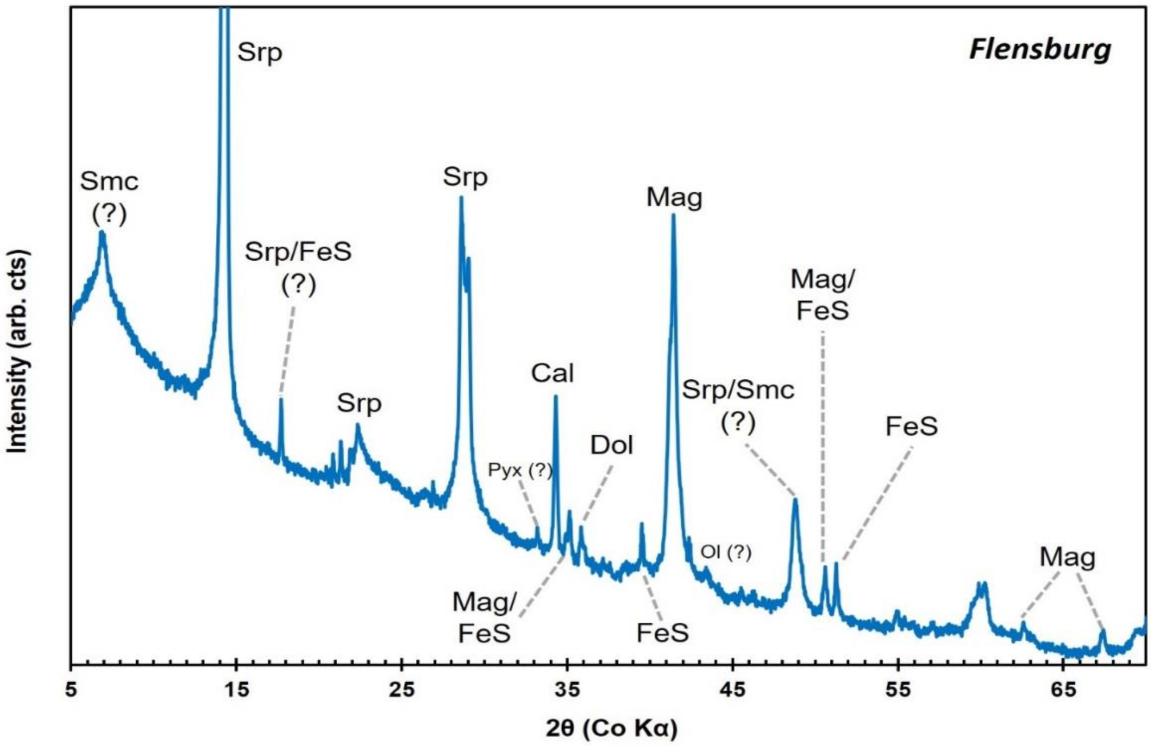

Fig. S16: XRD pattern of Flensburg collected using a PANalytical X'Pert Pro scanning XRD. Minerals identified include phyllosilicates (serpentine (Srp) and possibly smectite (Smc)), magnetite (Mag), Fe-sulphides (troilite and pyrrhotite (FeS)) and carbonates (calcite (Cal) and dolomite (Dol)). Olivine (Ol) and pyroxene (Pyx) may be present in low (<1%) abundances.

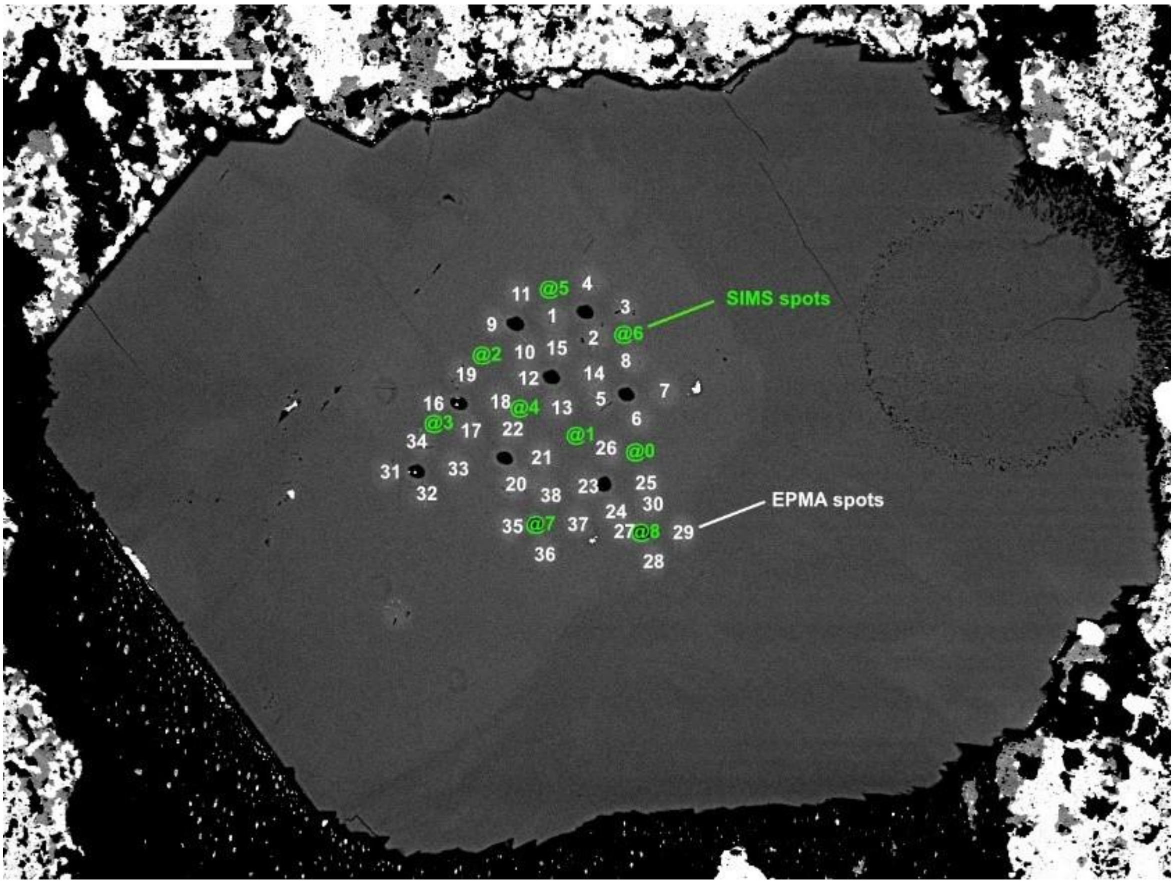

Fig. S17: BSE image of the HIGP calcite showing the analyzed EPMA spots (white numbers) and the SIMS spots (green, @). The analyses are restricted to a homogenous area and analyzed data can be found in Table S5a. The black holes are related to earlier SIMS analyses.

References-Supplement:

Akhmadaliev S., Heller, R., Hanf, D., Rugel, G., and Merchel, S. (2013) The new 6 MV AMS-facility DREAMS at Dresden, *Nucl. Instr. Meth. Phys. Res. B* **294**, 5-10.

Alexander C. M. O'D., Bowden R., Fogel M. L., Howard K. T., Herd C. D. K. and Nittler L. R. (2012) The provenances of asteroids, and their contributions to the volatile inventories of the terrestrial planets. *Science* **337**, 721-723.

Alexander C. M. O'D., Howard K., Bowden R. and Fogel M. L. (2013) The classification of CM and CR chondrites using bulk H, C and N abundances and isotopic compositions. *Geochim. Cosmochim. Acta* **123**, 244-260.

Amiguet E., Reynard, B., Caracas, R., Van de Moortele, B., Hilairet, N., and Wang Y. (2012) Creep of phyllosilicates at the onset of plate tectonics. *Earth and Planetary Science Letters* **345-348**, 142-150.

Barkan E., Musan I., and Boaz L. (2015) High-precision measurements of $\delta^{17}O$ and $^{17}O_{excess}$ of NBS19 and NBS18. *Rapid Communications in Mass Spectrometry* **29**, 2219–2224.

Barrat J.-A., Zanda B., Moynier F., Bollinger C., Liorzou C., and Bayron G. (2012) Geochemistry of CI chondrites: Major and trace elements, and Cu and Zn isotopes. *Geochimica et Cosmochimica Acta* **83**, 79-92.

Barrat J.-A., Rouxel O., Wang K., Moynier F., Yamaguchi A., Bischoff A., and Langlade J. (2015) Early stages of core segregation recorded by Fe isotopes in an asteroidal mantle. *Earth Planet. Sci. Lett*. **419**, 93–100.

Barrat J.-A., Gillet, P., Dauphas, N., Bollinger, C., Etoubleau, J., Bischoff, A., and Yamaguchi A. (2016) Evidence from Tm anomalies for non-CI refractory lithophile element proportions in terrestrial planets and achondrites. *Geochim. Cosmochim. Acta*. **176**, 1-17.

Bischoff A., Barrat J.-A., Bauer, K., Burkhardt, C., Busemann, H., Ebert, S., Gonsior, M., Hakenmüller, J., Haloda, J., Harries, D., Heinlein, D., Hiesinger, H., Hochleitner, R., Hoffmann, V., Kaliwoda, M., Laubenstein, M., Maden, C., Meier, M. M. M., Morlok, A., Pack, A., Ruf, A., Schmitt-Kopplin, P., Schönbächler, M., Steele, R. C. J., Spurny, P., and Wimmer K. (2017). The Stubenberg meteorite - an LL6 chondrite fragmental breccia recovered soon after precise prediction of the strewn field. *Meteoritics & Planetary Science* **52**, 1683-1703.

Bischoff A., Barrat J.-A., Berndt J., Borovicka J., Burkhardt C., Busemann H., Hakenmüller J., Heinlein D., Hertzog J., Kaiser J., Maden C., Meier M. M. M., Morino P., Pack A., Patzek M., Reitze M. P., Rüfenacht M., Schmitt-Kopplin P., Schönbächler M., Spurny P., Weber I., Wimmer K. and Zikmund T. (2019) The Renchen L5-6 chondrite breccia – the first confirmed meteorite fall from Baden-Württemberg (Germany). *Geochemistry – Chemie der Erde* **79**, 125525.

Brand A.B., Coplen T.B., Vogl J., Rosner M., and Prohasa T. (2014) Assessment of international reference materials for isotope-ratio analysis (IUPAC Technical Report). *Pure and Applied Chemistry* **86**(3), 425–467.

Brennecka G.A., Borg, L.E., Romaniello, S.J., Souders, A.K., Shollenberger, Q.R., Marks, N.E., and Wadhwa M. (2017) A renewed search for short-lived ^{126}Sn in the early Solar System: Hydride generation MC-ICPMS for high sensitivity Te isotopic analysis. *Geochimica et Cosmochimica Acta* **201**, 331-344.

Burkhardt C., Dauphas N., Tang H., Fischer-Gödde M., Qin L., Chen J. H., Rout S. S., Pack A., Heck P. R. and Papanastassiou D. A. (2017) In search of the Earth-forming reservoir: Mineralogical, chemical, and isotopic characterizations of the ungrouped achondrite NWA 5363/NWA 5400 and selected chondrites. *Meteorit. Planet. Sci.* **52**, 807–826.

Clayton R. N. (2008) Oxygen isotopes in the early Solar System - A historical perspective. In: MacPherson *et al.* (Eds.) *Oxygen in the solar system*. vol. **68**, American Mineralogical Society (Washington), p. 5-14.

Consolmagno G. J., Britt D. T., and Macke R. J. (2008) The significance of meteorite density and porosity. *Chemie der Erde* **68**, 1-29.

Donohue P.H., Huss G.R., and Nagashima K. (2019) New synthetic carbonates for investigation of manganese-chromium chronology by secondary ion mass spectrometry. *Lunar and Planetary Science Conference* **50**, #1959.

Dvorski S., Gonsior M., Hertkorn N., Uhl J., Müller H., Griebler C., and Schmitt-Kopplin P. (2016) Geochemistry of dissolved organic matter in a spatially highly resolved groundwater petroleum hydrocarbon plume cross-section. *Environmental Science & Technology* **50**(11), 5536–5546.

Fehr M.A., Rehkämper M., and Halliday A.N. (2004) Application of MC-ICPMS to the precise determination of tellurium isotope compositions in chondrites, iron meteorites and sulfides. *International Journal of Mass Spectrometry* **232**, 83-94.

Finocchi F. and Gail H.P. (1997) Chemical reactions in protoplanetary accretion disks. III. The role of ionisation processes. *Astronomy and Astrophysics* **327**, 825-844.

Gerber S., Burkhardt C., Budde G., Metzler K. and Kleine T. (2017) Mixing and transport of dust in the early solar nebula as inferred from titanium isotope variations among chondrules. *Astrophys. J.* **841**, L17.

Goodrich C. A., Kita N. T., Yin Q.-Z., Sanborn M. E., Williams C. D., Nakashima D., Lane M. D. and Boyle S. (2017) Petrogenesis and provenance of ungrouped achondrite Northwest Africa 7325 from petrology, trace elements, oxygen, chromium and titanium isotopes, and mid-IR spectroscopy. *Geochim. Cosmochim. Acta* **203**, 381–403.

Harries D. and Zolensky M.E. (2016) Mineralogy of iron sulfides in CM1 and CI1 lithologies of the Kaidun breccia: Records of extreme to intense hydrothermal alteration. *Meteoritics & Planetary Science* **51**, 1096–1109.

Hertkorn N., Harir M., and Schmitt-Kopplin Ph. (2015) Nontarget analysis of Murchison soluble organic matter by high-field NMR spectroscopy and FTICR mass spectrometry. *Magnetic Resonance Chemistry* **53**, 754-768.

Hilairet N., Reynard B., Wang Y., Daniel I., Merkel S., Nishiyama N., and Petitgirard S. (2007) High-pressure creep of serpentine, interseismic deformation, and initiation of subduction. *Science* **318**, 1910-1913.

Jull A. J. T., Cloudt S. and Cielaszyk E. (1998) ^{14}C terrestrial ages of meteorites from Victoria Land, Antarctica and the infall rate of meteorites. In Grady, M. M. et al. (eds) *Meteorites: Flux with time and impact effects.* Geological Society, London, Special Publication **140**, 75-91.

King A. J., Schofield P. F., Howard K. T., and Russell S. S. (2015) Modal mineralogy of CI and CI-like chondrites by Xray diffraction. *Geochimica et Cosmochimica Acta* **165**, 148–160.Kita N. T., Yin Q. Z., MacPherson G. J., Ushikubo T., Jacobsen B., Nagashima K., Kurashi E., Krot A., and Jacobsen S. B. (2013) ^{26}Al-^{26}Mgisotope systematics of the first solids in the early solar system. *Meteoritics and Planetary Science* **48**, 1383-1400.

Köhler M., Degering, D., Laubenstein, M., Quirin, P., Lambert, M.-O., Hult, M., Arnold, D., Neumaier, S., and Reyss J.-L. (2009) A new low-level ɣ-ray spectrometry system for environmental radioactivity at the underground laboratory Felsenkeller. *Applied Radiation and Isotopes* **67**, 736-740.

Korschinek G., Bergmaier A., Faestermann T., Gerstmann U. C., Knie K., Rugel G., Wallner A., Dillmann I., Dollinger G., Lierse von Gostomski Ch., Kossert K., Maiti M., Poutivtsev M., and Remmert A. (2010) A new value for the half-life of ^{10}Be by heavy-ion elastic recoil detection and liquid scintillation counting. *Nucl. Inst. Meth. Phys. Res.* **B 268**, 187-191.

Leya I. and Masarik, J. (2009) Cosmogenic nuclides in stony meteorites revisited. *Meteoritics & Planetary Science* **44**, 1061-1086.

Leya I., J.-C. David, T. Faestermann, M. Froehlich, N. Kivel, D. Koll, G. Korschinek, S. McIntyre, S. Merchel, S. Pavetich, G. Rugel, D. Schumann, T. Smith, and Wallner A. (2020) ^{53}Mn and ^{60}Fe in iron meteorites - new data and model calculations, *Meteorit. Planet. Sci.* **55**, 818-831.

Ludwig F., Wagner, L., Al-Abdullah, T., Barnaföldi, G.G., Bemmerer, D., Degering, D., Schmidt, K., Suranyi, G., Szücs, T., and Zuber K. (2019) The muon intensity in the Felsenkeller shallow underground laboratory. *Astroparticle Physics* **112**, 24-34.

Meija J., Coplen, T.B., Berglund, M., Brand, W.A., De Bièvre, P., Gröning, M., Holden, N.E., Irrgeher, J., Loss, R.D., Walczyk, T., and Prohaska T. (2016) Isotopic compositions of the elements 2013 (IUPAC Technical Report). Pure and Applied Chemistry 88(3): 293–306.

Merchel S. and Herpers U. (1999) An update on radiochemical separation techniques for the determination of long-lived radionuclides via accelerator mass spectrometry. *Radiochim. Acta* **84**, 215-219.

Meteoritical Bulletin Database (https://www.lpi.usra.edu/meteor)

Millet M.-A. and Dauphas N. (2014) Ultra-precise titanium stable isotope measurements by double-spike high resolution MC-ICP-MS. *J. Anal. At. Spectrom.* **29**, 1444-1458.

Nakazawa H. and Morimoto N. (1970) Pyrrhotite phase relations below 320 C. *Proceedings of the Japan Academy* **46**, 678–683.

Neumann W. and Kruse A. (2019) Differentiation of Enceladus and retention of a porous core. *The Astrophysical Journal* **882**, 47.

Neumann W., Breuer D., and Spohn T. (2014) Modelling of compaction in planetesimals. *Astronomy and Astrophysics* **567**, A120.

Neumann W., Breuer D., and Spohn T. (2015) Modelling the internal structure of Ceres: Coupling of accretion with compaction by creep and implications for the water-rock differentiation. *Astronomy and Astrophysics* **584**, A117.

Neumann W., Jaumann R., Castillo-Rogez J., Raymond C., and Russell C.T. (2020) Ceres' partial differentiation: undifferentiated crust mixing with a water-rich mantle. *Astronomy and Astrophysics* **633**, A117.

Niese S., Köhler M., and Gleisberg B. (1998) Low-level counting techniques in the underground laboratory "Felsenkeller" in Dresden. *Journal of Radioanalytical and Nuclear Chemistry* **233**, 167-172.

Norris T. L., Gancarz A. J., Rokop D. J., and Thomas K. W. (1983) Half-life of ^{26}Al. *Proc. of the 14th Lunar and Planetary Science Conference, Journal of Geophysical Research Suppl.* **8**, B331-B333.

Pack A., Tanaka R., Hering M., Sengupta S., Peter, S., and Nakamura E. (2016) The oxygen isotope composition of San Carlos olivine on VSMOW2-SLAP2 scale, *Rapid Communications in Mass Spectrometry* **30**: 1495-1504.

Passey B. H., Hu H., Ji H., Montanari S., Li S., Henkes G.A., and Levin N.E. (2014) Triple oxygen isotopes in biogenic and sedimentary carbonates. *Geochimica et Cosmochimica Acta* **141**, 1–25.

Paul M., Ahmad I., and Kutschera W. (1991) Half-life of ^{41}Ca. *Z. Phys. A - Hadrons and Nuclei* **340**, 249-254.

Peters S.T., Alibabaie, N., Pack, A., McKibbin, S.J., Raeisi, D., Nayebi, N., Torab, F., Ireland, T., and Lehmann B. (2020) Triple oxygen isotope variations in magnetite from iron-oxide deposits, central Iran, record magmatic fluid interaction with evaporite and carbonate host rocks. *Geology* **48**, 211-215.

Popova O. P., P. Jenniskens, V. Emel'yanenko, A. Kartashova, E. Biryukov, S. Khaibrakhmanov, V. Shuvalov, Y. Rybnov, A. Dudorov, V. I. Grokhovsky, D. Badyukov, Q.-Z. Yin, P. S. Gural, J. Albers, M. Granvik, L. G. Evers, J. Kuiper, V. Kharlamov, A. Solovyov, Y. S. Rusakov, S.

Korotkiy, I. Serdyuk, A. V. Korochantsev, M. Y. Larionov, D. Glazachev, A. E. Mayer, G. Gisler, S. V. Gladkovsky, J. Wimpenn, M. E. Sanborny, A. Yamakawa, K. L. Verosub, D. J. Rowland, S. Roeske, N. W. Botto, J. M. Friedrich, M. E. Zolensky, L. Le, , K. Ziegler, T. Nakamura, I. Ahn, J. Ik Lee, Q. Zhou, X.-H. Li, Q.-L. Li, Y. Liu, G.-Q. Tang, T. Hiroi, D. Sears, I. A. Weinstein, A. S. Vokhmintsev, A. V. Ishchenko, Ph. Schmitt-Kopplin, N. Hertkorn, K. Nagao, M. K. Haba, M. Komatsu, and T. Mikouchi, (the Chelyabinsk Airburst Consortium) (2013) Chelyabinsk airburst, damage assessment, meteorite recovery, and characterization. *Science* **342,** 1069-1073.

Qin L., Alexander C. M. O., Carlson R. W., Horan M. F., and Yokoyama T. (2010) Contributors to chromium isotope variation of meteorites. *Geochimica et Cosmochimica Acta* **74**, 1122–1145.

Rugel G., Pavetich S., Akhmadaliev S., Enamorado Baez S.M., Scharf A., Ziegenrücker R., and Merchel S. (2016) The first four years of the AMS-facility DREAMS: Status and developments for more accurate radionuclide data, *Nucl. Instr. Meth. Phys. Res.* **B 370**, 94-100.

Sanborn M. E., Wimpenny J., Williams C. D., Yamakawa A., Amelin Y., Irving A. J. and Yin Q.-Z. (2019) Carbonaceous achondrites Northwest Africa 6704/6693: Milestones for early Solar System chronology and genealogy. *Geochim. Cosmochim. Acta* **245**, 577–596.

Schmitt-Kopplin Ph., Gabelica, Z., Gougeon, R.D., Fekete, A., Kanawati, B., Harir, M., Gebefuegi, I., Eckel, G., and Hertkorn N. (2010) High molecular diversity of extraterrestrial organic matter in Murchison meteorite revealed 40 years after its fall. *PNAS*, **107**(7), 2763-2768.

Schumann D., Kivel N., and Dressler R. (2019) Production and characterization of ^{60}Fe standards for Accelerator Mass Spectrometry, *PloS ONE* **14**(6), e0219039.

Schwenn M. B. and Goetze C. (1978) Creep of olivine during hot pressing. *Tectonophysics* **48**, 41-60.

Sessions A. L., Burgoyne T. W., and Hayes J. M. (2001) Determination of the H-3 factor in hydrogen isotope ratio monitoring mass spectrometry. *Analytical Chemistry* **73**, 200-207.

Sharp Z.D., Gibbons, J.A., Atudorei, V., Pack, A., Sengupta, S., Shock, E.L., and Knauth L.P. (2016) A calibration of the triple oxygen isotope fractionation in the SiO_2–H_2O system and applications to natural samples. *Geochimica et Cosmochimica Acta* **186**, 105-119.

Shukolyukov A., and Lugmair G. W. (2006) Manganese–chromium isotope systematics of carbonaceous chondrites. *Earth and Planetary Science Letters* **250**, 1-2, 200-213.

Śliwiński M. G., Kitajima K., Kozdon R., Spicuzza M. J., Fournelle J. H., Denny A., and Valley J. W. (2016a) Secondary ion mass spectrometry bias on isotope ratios in dolomite–ankerite, Part I: d^{18}O matrix effects. *Geostandards and Geoanalytical Research* **40**, 157–172.

Śliwiński M. G., Kitajima K., Kozdon R., Spicuzza M. J., Fournelle J. H., Denny A., and Valley J. W. (2016b) Secondary ion mass spectrometry bias on isotope ratios in dolomite–ankerite, Part II: d^{13}C matrix effects. *Geostandards and Geoanalytical Research* **40**, 173–184.

Steele R.C.J., Heber V.S., and McKeegan K.D. (2017) Matrix effects on the relative sensitivity factors for manganese and chromium during ion microprobe analysis of carbonate: Implications for early Solar System chronology. *Geochimica et Cosmochimca Acta* **201**, 245–259.

Tang H. and Dauphas N. (2012) Abundance, distribution, and origin of ^{60}Fe in the solar protoplanetary disk. *Earth and Planetary Science Letters* **359**, 248-263.

Trinquier A., Elliott T., Ulfbeck D., Coath C., Krot A. N. and Bizzarro M. (2009) Origin of nucleosynthetic isotope heterogeneity in the solar protoplanetary disk. *Science* **324**, 374–376.

Trinquier A., Birck J. L., Allègre C. J., Göpel C., and Ulfbeck D. (2008a) ^{53}Mn–^{53}Cr systematics of the early Solar System revisited. *Geochimica et Cosmochimica Acta* **72**, 5146–5163.

Trinquier A., Birck J.-L., and Allègre C. J. (2008b) High-precision analysis of chromium isotopes in terrestrial and meteorite samples by thermal ionization mass spectrometry. *Journal of Analytical Atomic Spectrometry* **23**, 1565-1574.

Tyra M., Brearley A., and Yunbin G. (2016) Episodic carbonate precipitation in the CM chondrite ALH 84049: An ion microprobe analysis of O and C isotopes. *Geochimica et Cosmochimica Acta* **175**, 195–207.

Van Schmus W. R. (1995) Global Earth Physics. AGU Reference Shelf 1 (American Geophysical Union). Chapter A Handbook on Physical Constants. pp. 283-291.

Vermeesch P. (2018) IsoplotR: A free and open toolbox for geochronology. *Geoscience Frontiers* **9**, 1479–1493

Waldner P. and Pelton A.D. (2004) Critical thermodynamic assessment and modeling of the Fe-Ni-S system. *Metall. and Materials Trans. B* **35**, 897–907.

Wallner A., Bichler, M., Buczak, K., Dressler, R., Fifield, L. K., Schumann, D., Sterba, J. H., Tims, S. G., Wallner, G., and Kutschera W. (2015) Settling the half-life of ^{60}Fe: fundamental for a versatile astrophysical chronometer. *Physical Review Letters* **114**, 041101.

Wallner A., Feige J., Kinoshita N., Paul M., Fifield L. K., Golser R., Honda M., Linnemann U., Matsuzaki H., Merchel S., Rugel G., Tims S. G., Steier P., Yamagata T., and Winkler S. R. (2016) Recent near-Earth supernovae probed by global deposition of interstellar radioactive ^{60}Fe. *Nature* **532,** 69–72.

Weber I., Morlok, A., Grund, T., Bauch, K. E., Hiesinger, H., Stojic, A., Grumpe, A., Wöhler, C., Klemme, S., Sohn, M., Martin, D. J. P., and Joy K. H. (2018) A mid-infrared reflectance database in preparation for space missions. *Lunar Planet. Sci. Conf.* **48**, #1430.

Williams N. H. (2015) *The origin of titanium isotopic anomalies within solar system material.* PhD thesis, University of Manchester.

Wostbrock J. A., Cano E. J., and Sharp Z. D. (2020) An internally consistent triple oxygen isotope calibration of standards for silicates, carbonates and air relative to VSMOW2 and SLAP2. *Chemical Geology* **533**: 119432.

Yamakawa A., Yamashita K., Makishima A., and Nakamura E. (2009) Chemical separation and mass spectrometry of Cr, Fe, Ni, Zn, and Cu in terrestrial and extraterrestrial materials using thermal ionization mass spectrometry. *Anal.Chem* **8**, 9787–9794.

Zhang J., Dauphas N., Davis A. M., and Pourmand A. (2011) A new method for MC-ICPMS measurement of Ti isotopic composition: identification of correlated isotope anomalies in meteorites. *J. Anal. At. Spectrom.* **26**, 2197-2205.

Zhang J., Dauphas N., Davis A. M., Leya I. and Fedkin A. (2012) The proto-Earth as a significant source of lunar material. *Nature Geoscience* **5**, 251–255.

Zolensky M. E., Ivanov A. V., Yang S. V., Mittlefehldt D. W., and Ohsumi K. (1996) The Kaidun meteorite: Mineralogy of an unusual CM1 lithology. *Meteoritics & Planetary Science* **31**, 484-493.